An internal solitary wave forecasting model in the northern South China Sea (ISWFM-NSCS)

Yankun Gong[1], Xueen Chen[2], Jiexin Xu[1], Jieshuo Xie[1], Zhiwu Chen[1], Yinghui He[1], Shuqun Cai[1,3,4]

[1]State Key Laboratory of Tropical Oceanography, South China Sea Institute of Oceanology, Chinese Academy of Sciences, Guangzhou 510301, China

[2]College of Oceanic and Atmospheric Sciences, Ocean University of China, Qingdao, 266100, China

[3]Institution of South China Sea Ecology and Environmental Engineering, Chinese Academy of Sciences, Guangzhou 510301, China

[4]University of Chinese Academy of Sciences, Beijing, 100049, China

Correspondence to: Shuqun Cai (caisq@scsio.ac.cn)

Abstract. Internal solitary waves (ISWs) are a ubiquitous phenomenon in the dynamic ocean system, which play a crucial role in driving transport through turbulent mixing. Over the past few decades, numerical modelling became a vital approach to investigate the generation mechanism and spatial distribution of ISWs. The northern South China Sea (NSCS) has been treated as a physical oceanographic focus of ISWs in massive numerical studies since last century. However, there was no systematic evaluation of a reliable three-dimensional (3D) model about accurately reproducing ISW characteristics in the NSCS. In this study, we implement a 3D ISW forecasting model in the NSCS and quantitatively evaluate the requirements of factors (i.e., model resolution, tidal forcing, and stratification selection) in accurately depicting ISW properties by comparing with observational data at a mooring station in the vicinity of the Dongsha Atoll. Firstly, the 500 m-resolution model can basically reproduce the principal ISW characteristics, while the 250 m-resolution model would be a better solution to identify wave properties, specifically increasing 40% accuracy of predicting characteristic half-widths. Nonetheless, a 250 m-resolution model spends nearly fivefold computational resources of a 500 m-resolution model in the same model domain. Compared with the former two, the model with a lower resolution of 1000 m severely underestimates the nonlinearity of ISWs, resulting in an incorrect ISW field in the NSCS. Secondly, the model with eight (or thirteen) primary tidal constituents can accurately reproduce the real ISW field in the NSCS, while the one with four main harmonics (M2, S2, K1 and O1) would underestimate averaged wave-induced velocity for about 38% and averaged mode-1 wave amplitude for about 15%. Thirdly, the model with the initial condition of field-extracted stratification gives a better performance in predicting some wave properties than the model with climatological stratification, namely 13% improvement of arrival time and 46% improvement of characteristic half-width. Finally, background currents, spatially varying stratification and external (wind) forcing are discussed to reproduce a more realistic ISW field in the future numerical simulations.

1 Introduction

Numerical simulations, one of the most important approaches to investigate internal solitary waves (ISWs) in the world's oceans, have been gradually developed from two-dimensional (2D, e.g., Du et al., 2008; Buijsman et al., 2010) to three-dimensional (3D, e.g., Zhang et al., 2011; Alford et al., 2015) over the past few decades. South China Sea (SCS), the largest marginal sea in the northwest Pacific, has been commonly known as an active region of ISWs via massive in-situ observations (cf. Ramp et al., 2004, 2019; Farmer et al., 2009, 2011) and numbers of remote sensing images (cf. Liu et al., 2004; Zheng et al., 2001, 2007). Although the vertical structure and horizontal distribution on the sea surface of ISWs can be nicely illustrated by field measurements at sparse sites and satellite images, respectively, they are still of limited value for telling a complete story of ISWs in the entire northern SCS (NSCS). Complementary to in-situ and remote-sensing observations, numerical model can give a comprehensive characterization in the ISW field in case of realistic initial and boundary conditions. Hence, we take NSCS as an example to introduce a high-performance ISW forecasting model and quantitatively evaluate requirements of model configurations (i.e., resolution, tidal forcing, and stratification selection) for accurately reproducing a real ISW field.

With the development of higher performance computing facilities, a variety of 3D realistic numerical models with structured and unstructured grids were established for simulating ISWs in the NSCS (see Table 1), such as MITgcm (Vlasenko et al., 2010), SUNTANS (Zhang et al., 2011) and FVCOM (Lai et al., 2019). Meanwhile, the model capabilities have been continuously improved (Simmons et al., 2011). Specifically, the model resolution was effectively enhanced from 250-1000 (Δx-Δy) m (Guo et al., 2011) in a limited domain to 150/300 m in a large domain including the entire NSCS (Zeng et al., 2019). From past to present, the barotropic tidal forcing dataset TOPEX/Poseidon Solution (TPXO, Egbert and Erofeeva, 2002) and climatological stratification dataset World Ocean Atlas (WOA, Locarnini et al., 2018) have been updated with higher resolutions both in horizontal and vertical, providing more realistic and precise boundary and initial conditions in the model configurations. Although it is commonly known that a higher-resolution model can tell a more complete story of ISWs, the usage of computational resources is worthy to be considered. Thus, what resolution of model is needed to give an accurate depiction of ISW fields and simultaneously save the computational cost is still a question.

Even though numbers of previous in-situ observations have shown the four barotropic tidal constituents (M2, K1, O1 and S2) are dominant at the Luzon Strait (Zhao and Alford, 2006; Farmer et al., 2009), the other barotropic tidal constituents (e.g., N2, K2, P1 and Q1) are also non-negligible (Beardsley et al., 2004). Historically, numerical simulations with different numbers of tidal constituents have been widely employed to investigate the physical dynamics of ISWs in the NSCS, i.e., single K1 harmonic (Li, 2014), four tidal harmonics (Buijsman et al., 2010), and eight primary tidal harmonics (Alford et al., 2015; Jin et al., 2021). Among these, eight tidal constituents were most commonly applied in the 3D models. However, other tidal constituents, such as M4, MS4, MN4, MM, and MF, were yet to be considered. The questions are whether a single tidal constituent can reproduce a real ISW field and, if not, how many tidal constituents are required for running an accurate 3D realistic ISW model.

62 Apart from resolution and tidal forcing, stratification selection is also an important factor in improving model accuracy. A

63 horizontally homogenous stratification profile was normally implemented as an initial condition in a 3D realistic model (cf.

64 Zhang et al., 2011; Lai et al., 2019). Specifically, a domain average of the climatological dataset (WOA) is one of the most

65 common options (Vlasenko et al., 2010; Zeng et al., 2019), since the in-situ observational data are relatively inaccessible. Once

66 the field data at an isolated mooring station are available, are they a better choice than the climatological data to be the model's

67 initial condition? What if the mooring is near-field (in the vicinity of the Luzon Strait, the ISW generation site) or far-field

68 (e.g., in the deep basin or over the continental slope and shelf)?

69 In this paper, we attempt to introduce a high-performance ISW forecasting model and evaluate the roles of different

70 resolutions, initial and boundary conditions in accurately reproducing ISWs via a series of sensitivity 3D non-hydrostatic

71 numerical simulations. The paper is structured as follows. In section 2, configurations of the 3D forecasting model are

72 introduced, as well as the simultaneous remote sensing images and in-situ observations. The model calibrations are presented

73 in section 3. In section 4, we quantitatively illuminate the requirements of model resolutions, tidal constituents, and initial

74 stratification selection for a reliable 3D ISW forecasting model. Discussion and conclusions follow in section 5.

75 2 Data and Methods

76 To characterize the real ISW field in the NSCS, we implement an ISW forecasting model (ISWFM-NSCS) and compare the

77 modelled wave properties on the continental slope with those observed at in-situ mooring station DS (marked as magenta star

78 in Fig. 1a). Remote sensing images are downloaded for the model calibration as well.

79 2.1 Numerical modelling

80 Although running a 2D slice model is much more economical than running a 3D model from the perspective of

81 computational resources, the 2D model cannot correctly reproduce the ISW field in the real ocean (see Appendix A). Therefore,

82 we implement a realistic 3D non-hydrostatic primitive equation ocean solver (MIT general circulation model, MITgcm,

83 Marshall et al., 1997) in the spherical coordinate to reproduce the ISWs features in the NSCS. The model domain (115.8º –

84 123.8ºE, 17.8º – 22.3ºN, see blue box in Fig. 1a) includes the main generation site of ISWs (i.e., Luzon Strait) and the mooring

85 station DS on the continental slope. Bathymetry data are derived from the global gridded bathymetry dataset GEBCO

86 (https://www.gebco.net/data_and_products/gridded_bathymetry_data). To keep the consistency with the instrumental

87 deploying period, we start the model from 00:00 UTC 5 August 2014 and last fifteen days. Previous statistical analyses, based

88 on SAR images in the NSCS from 1995 to 2001, also indicated that ISW occurrence frequencies were relatively high in August

89 (Zheng et al., 2007). The initial model temperature and salinity profiles (see black and blue lines in Fig. 1b) are derived from

90 the WOA18 climatology dataset (World Ocean Atlas 2018) by spatially averaging the monthly output in August, resulting in

91 horizontally-uniform conditions. Density and buoyancy frequency profiles are shown as black lines in Figs. 1c and 1d.

92  To ensure ISWs can be physically derived and consider the computational efficiency, the horizontal cell (Δx) is set as 500

93 m in both zonal and meridional directions. In order to satisfy the high-mode vertical resolution requirements, 90 vertical layers

94 are spaced in accordance with the hyperbolic tangent function (Stewart et al., 2017), namely ranging from 5 m near the surface

95 to 120 m near the sea bed (in the deep water). We impose a time step of $\Delta t = 10$ sec to satisfy the Courant-Friedrichs-Lewy

96 (CFL) conditions in both horizontal and vertical. The Coriolis parameter is varying with latitudes in the entire model domain.

97 To determine whether non-hydrostatic mode is necessary, we also run a hydrostatic model (not shown). It is noting that fake

98 internal solitary-like wave trains, also called spurious non-hydrostatic processes (Alvarez et al., 2019), are clearly visible at

99 first glance, suggesting that hydrostatic mode is inappropriate for a high-resolution model of ISWs. We therefore configure

100 the model in non-hydrostatic mode.

101  The control run (Exp. 1, **500m_8HARs**) is driven by eight main tidal constituents (M2, S2, N2, K2, K1, O1, P1, and Q1) on

102 the four open boundaries with values originated from the Oregon State University TOPEX/Poseidon Solution (TPXO8-atlas

103 data) with 1/30º resolution (Egbert and Erofeeva, 2002). A 25 km wide sponge layer is imposed on each lateral boundary to

104 absorb internal wave energy and avoid wave reflection back to the inner region. Quasi-steady conditions occur after 3 days

105 (see Appendix B), so the model results are analyzed over the remaining 12 days (8 – 20 August). The sampling rate of model

106 outputs is 1 h interval for the entire model domain in the control run (**500m_8HARs**) and single-point outputs with a higher

107 sampling rate of 1 min at the selected station DS for recording the local ISW properties, and thereby comparing to the in-situ

108 observations. Constant horizontal and vertical eddy viscosity and diffusivity coefficients are imposed as $A_h = 0.5$ m^2 s^{-1}; $A_v =$

109 5×10^{-3} m^2 s^{-1}; $K_h = 0.5$ m^2 s^{-1}; $K_v = 5 \times 10^{-3}$ m^2 s^{-1} to eliminate grid-scale instability (Legg and Huijts, 2006). The bottom

110 stresses are parameterized using a quadratic law with a bottom drag coefficient of $C_d = 2.5 \times 10^{-3}$.

111 **2.2 Remote sensing images**

112  Remote sensing imagery contains lots of detailed information of ISW properties, including wave crest lines and their arrival

113 time, which was commonly applied in the NSCS (Liu et al., 2004; Zheng et al., 2007). Here we download two MODIS true-

114 color pictures with a horizonal resolution of 250 m at 05:15 UTC on 14 August and at 02:50 UTC on 15 August 2014,

115 respectively. In addition, we compute the horizontal gradients of sea surface height ($|\nabla \eta|$, in the unit of cm km^{-1}), which detects

116 the variations in surface roughness caused by the ISW-induced convergent and divergent currents, thereby producing

117 analogous images to the satellite images. Note that the model is hourly sampled, so we select the closest snapshots of $|\nabla \eta|$ at

118 05:00 UTC on 14 August and at 03:00 UTC on 15 August 2014 to compare with MODIS images.

119 **2.3 In-situ measurements**

120  The through-water-column mooring station DS (magenta star in Fig. 1a) is located at 117º44.7'E, 20º44.2'N in the vicinity

121 of the Dongsha Atoll, which was deployed at a water depth of ~1250 m from 1 August to 28 September 2014. Three acoustic

122 Doppler current profilers (ADCPs) measured currents ranging from a depth of 1180 m to the sea surface every two minutes

123 with 16-m vertical bins in upper 900 m and 8-m vertical bins below 900 m. The mooring was configured by temperature

124 sensors, a conductivity-temperature-depth (CTD) sensor and conductivity-temperature (CT) sensors at different water depths.

125 The temperature sensors were at 10 m, 30 m, 50 m, 90 m, 130 m, 150 m, 170 m, 250 m, 350 m, 500 m, 600 m, 700 m, 800 m,

126 950 m, 1050 m, and 1220 m, respectively; the CTD sensor was at 1100 m; and the CT sensors were at 20 m, 40 m, 70 m, 110

127 m, 150 m, 200 m, 300 m, 450 m, 550 m, 650 m, 750 m, 850 m, 1000 m, and 1200 m, respectively. Temporal sampling rates

128 were 10 sec for the temperature and CTD sensors, and 15 sec for the CT sensors, respectively. The instruments carried by the

129 moorings generally functioned well, but CT sensors stopped working after 6 September 2014 due to the lack of power. Besides,

130 Xu et al. (2020) indicated that an anti-cyclonic eddy dominated the region of the mooring since mid-September 2014, which

131 significantly affected the local wave properties at the DS station. To avoid the impacts of background currents, we selected

132 fifteen ISWs during the spring tidal period from 00:00 UTC 8 August to 00:00 UTC 15 August as criteria to quantitatively

133 evaluate the performance of sensitivity numerical experiments.

134 3 Model results and calibrations

135 In this section, we validate the model accuracy from three aspects: barotropic tidal constituents via comparing with TPXO8-

136 atlas dataset and in-situ observational data; spatial distributions of ISWs via comparing with the remote-sensing images; wave

137 properties (i.e., amplitude, arrival time, wave-induced velocity and propagation direction) of ISWs via comparing with the in-

138 situ observations at mooring station DS.

139 3.1 Barotropic tide calibrations

140 The 3D control run only runs for 15 days, which is too short to do the harmonic analysis. To validate the model accuracy in

141 simulating the barotropic currents of eight key tidal constituents, we rerun a 3D model (Exp. 2, **500m_8HARs_BT**) with the

142 same configurations as **500m_8HARs**, but extend the duration time to 100 days and turn off the iteration of temperature and

143 salinity to focus on the barotropic tide regimes.

144 As M2, S2, K1, and O1 barotropic tides are dominant in the NSCS (Ramp et al., 2004; Farmer et al., 2009), here we calculate

145 the amplitude (U) and phase (ϕ) of the zonal velocity ($\boldsymbol{u_{bt}}$) by doing the harmonic analysis over the last 90 days in Exp. 2

146 (**500m_8HARs_BT**) and compare them with the TPXO8-atlas dataset. A root-mean-square error ($RMSE$), referring to

147 Cummins and Oey (1997), is computed to evaluate the model performance in the barotropic regime, which is given by

$$148 \quad RMSE_h = \sqrt{\frac{1}{2}[(U_m^2 + U_o^2) - U_m U_o \cos(\phi_m - \phi_o)]}, \quad (1)$$

149 in which, subscript h represent four different harmonics; U and ϕ are amplitude and phase of zonal barotropic currents with

150 the subscripts m for model and o for observation (TPXO8-atlas). We therefore obtain the horizontal distributions of $RMSE$

151 for four tidal constituents (see Figs. 2a – 2d). In most model domain, $RMSE$ is less than 0.02 m s^{-1}, but slightly larger in the

152 shallow water (e.g., Luzon Strait and the continental shelf), which is still less than 0.2 m s^{-1}. It may be because that the

153 bathymetry derived from the GEBCO dataset and resolutions in our model differ from those in the TPXO8-atlas, thereby

154 resulting in the discrepancy.

155   In addition to comparison between this model and the global tide model, we extract the DS station outputs with a high

156 sampling rate for comparing with the in-situ observations. To avoid the effects of massive high-frequency motions (i.e.,

157 environmental noises) in the observational time series on the barotropic regime, we first do the harmonic analysis for zonal

158 barotropic velocities from 5 August to 19 September, then extract the amplitude and phase of eight key tidal constituents, and

159 restructure the time series (see red line in Fig. 2e). In terms of the model results, we obtain the time series at station DS in the

160 same way (see black line in Fig. 2e). It is worth mentioning that the discrepancy between the eight-harmonic restructured time

161 series and the raw data in the model is small, since the experiment is basically driven by the eight tidal constituents and does

162 not include any affects from the background environment. By comparing the two timeseries, the model reliability is validated

163 all through the spring and neap tides. Overall, the model presents nice performance in the barotropic regime.

3.2 Comparison with MODIS images

164

165   Apart from the model validation in barotropic tides, we then look over the control run (***500m_8HARs***) in baroclinic (ISWs)

166 regime by comparing the model results with MODIS images. Figs. 3a and 3b both show two successive ISWs (labeled as IW1

167 and IW2) in the deep basin with a distance of ~120 km. The lengths, curvatures and locations of IW1 and IW2 in the simulation

168 are consistent with those in the MODIS image. However, two other ISWs occurring over the continental slope and shelf are

169 captured in the numerical simulations, but not observed on 14 August in the MODIS-Aqua image due to the cloud covering

170 (Fig. 3b). Conversely, the cloud disappeared on 15 August, so the MODIS-Terra sensor gives a clear seascape painting of

171 ISWs both in the shallow water (i.e., IW2) and deep water (i.e., IW3 and IW4). Note that IW2 in Figs. 3b and 3d are the same

172 ISW, which propagates ~250 km within 19 hours and 35 mins. All ISWs (IW2, IW3 and IW4) in Figs. 3c and 3d occur at the

173 fairly close locations with analogous wave properties. From the perspective of crestline lengths, the numerical model shows

174 well agreement with the MODIS images, namely 131 km versus 133 km for IW2 in Figs. 3a and 3b; 187 km versus 198 km

175 for IW3 and 74 km versus 69 km for IW4 in Figs. 3c and 3d. Note that the sea surface gradients ($|\nabla \eta|$) larger than 2 cm km^{-1}

176 along the crestlines are extracted and defined as the crestline lengths of NLIWs. Besides, in the water depth shallower than

177 500 m, the modelled IW2 exhibits an ISW train with trailing waves, which is also shown in the MODIS image. As the model

178 neglects wind above the sea surface and other marine dynamical processes, there are still some subtle nuances of wave

179 characteristics between them. Overall, this model nicely demonstrates spatial distributions of ISWs in the NSCS, based on the

180 comparison with remote sensing imagery.

3.3 Comparison with in-situ observations

181

182   To further evaluate the model performance in reproducing ISWs, we introduce the in-situ observations. The vertical structure

183 and timing of the wave arrivals, after crossing the deep basin, can be seen in details using daily plots (Figs. 4a – 4g) of the

184   temperature isotherms and baroclinic (ISW-induced) velocities from 8 to 14 August at mooring DS. For clarity, only the results

185   in upper 900 m are shown in Fig. 4, including the main wave-induced temperature fluctuations. On the basis of space-time

186   diagram of isopycnal displacements along the main propagation paths of ISWs (not shown), the averaged nonlinear internal

187   wave speeds are ~3.0 m s^{-1} from the Luzon Strait to the deep basin, so it takes roughly 1.5 days for ISWs to propagate from

188   the generation site to the targeted station (DS). We move the arrival time (i.e., 00:00 UTC 8 August - 00:00 UTC 14 August)

189   of ISWs 1.5 days forward at the station DS, so the related barotropic tides gradually increase during the spring tidal cycle at

190   the Luzon Strait (i.e., 12:00 UTC 6 August - 12:00 UTC 12 August). It explains why ISWs were relatively weak and linear

191   from 8 to 10 August (Figs. 4a – 4c), but became significant and nonlinear from 11 to 14 August (Figs. 4d – 4g). A single ISW

192   was captured around 12:00 UTC from 11 to 14 August, which arrived at the location at approximately the same time every

193   day (termed as type-a ISWs by Ramp et al. (2004)). Meanwhile, a wave train, consisted of two dominant solitons and some

194   small trailing waves, arrived at the station an hour later each day, showing the same wave characteristics as type-b ISWs in

195   Ramp et al. (2004).

196   In terms of the model, we also use the daily plots (Figs. 4h – 4n) at station DS with 1 min sampling rate to show its similarity

197   to the in-situ observations. An increasing trend of wave amplitude and nonlinearity is obvious from 8 August to 14 August in

198   the model results, suggesting precise depictions of barotropic tides and ISWs' characteristics. Specifically, both type-a (single

199   solitons) and type-b ISWs (wave trains) are displayed with analogous arrival time, wave-induced (baroclinic) velocity (color

200   shades in Fig. 4) and wave amplitude (contours in Fig. 4) to those in the observations. It's worth noting that even the linear

201   internal tides and/ or hydraulic jumps around 12:00 UTC from 8 to 10 August are reproduced. Although the model omits some

202   small wave signals (see blue arrows in Fig. 4e) in the observations, which might be induced by non-tidal processes such as

203   background currents, the model still shows a well performance in the ISW reproduction.

204   To quantitatively identify the model accuracy, we select fifteen ISWs (marked as red arrows in the left column of Fig. 4),

205   extract their wave properties (i.e., arrival time, maximum wave-induced velocity, propagation direction and maximum mode-

206   1 wave amplitude) and compare between in-situ observations and numerical simulations. We obtain wave propagation

207   direction by computing the angle of baroclinic zonal and meridional components in the layer with maximum velocity. The

208   maximum mode-1 wave amplitude (A_1) is extracted from the mooring data and model outputs by least squares fitting density

209   perturbation profiles $\rho'(z)$ to normalized modal structure function $W_n(z)$, following the similar procedures to those described

210   by Buijsman et al. (2010) and Rayson et al. (2012). Although the mode-1 wave amplitude can also be extracted by least squares

211   fitting the horizontal baroclinic velocity, Rayson et al. (2019) suggested that the method in velocity field was fuzzy with

212   unidirectional internal waves. The modal structure function can be resolved by a shear-free Taylor-Goldstein equation with

213   the background stratification $N^2(z)$, which is given by

$$\frac{d^2W_n(z)}{dz^2} + \frac{N^2(z)}{c_n}W_n(z) = 0, \tag{2}$$

215   with the boundary conditions $W_n(0) = W_n(-H) = 0$. Subscript n represents the mode number and c_n is the phase speed of

216   the linear internal waves in n^{th} mode. The buoyancy perturbation $b(z)$, depending on density perturbation $\rho'(z)$, is written as

$$b(z) = -g \frac{\rho'(z)}{\rho_0}, \qquad (3)$$

218   in which, ρ_0 is the reference density. Following the internal wave polarization relationships (Gerkema and Zimmerman,
219   2008), we fit the wave amplitudes (A_n) in different vertical modes to $b(z)$ in both in-situ observations and numerical
220   simulations via

$$b(z) = \sum_{n=1}^{5} A_n N^2(z) W_n(z), \qquad (4)$$

222   Here, we select the first five vertical modes ($n = 1 - 5$) to do the least squares fitting and mainly discuss the mode-1 wave
223   amplitude (A_1) due to its significant dominance (Fig. 4).

224   According to the above approaches, we extract the four wave properties for fifteen ISWs and plot Fig. 5, in which
225   observation and model results are shown in red and green, respectively. First, we list the arrival time of ISWs on the two sides
226   of Fig. 5. The bias between observation and model is always smaller than 1.5 h and the root mean square deviation (RMSD)
227   is 0.71 h, indicating accurate depiction of ISW arrival time in the control run (**500m_8HARs**). Second, the maximum baroclinic
228   velocity (Fig. 5a) and the averaged values (0.98 m s^{-1} and 1.18 m s^{-1}, respectively) are shown in the solid lines. It is suggested
229   that the model underestimates the baroclinic velocity due to neglect of some background non-tidal signals, thereby introducing
230   a RMSD of 0.41 m s^{-1}. Third, the averaged propagation directions of ISWs are ~285º and ~291º, respectively
231   (the angle measured counterclockwise from north) in the model results and observational data with a RMSD of 8.35º. It is
232   worth mentioning that the type-a ISWs mainly propagate westward while the type-b ISWs propagate north-westward in both
233   observation and model, verifying the model's reliability to some extent. Finally, the averaged maximum mode-1 wave
234   amplitude (~108 m) in the model is close to that (~99 m) in the observation. Nonetheless, the RMSD of mode-1 wave amplitude
235   is 37.27 m. Overall, the control run can basically reproduce various wave properties of ISWs observed in the vicinity of the
236   Dongsha Atoll in the NSCS.

4 Assessment of factors affecting 3D model forecasting precision

238   In this section, based on the control run, we alter the model configurations, such as the requirements of horizontal resolutions,
239   numbers of tidal constituents and initial stratification, to respectively estimate their effects on the model forecasting precision
240   of ISWs in the NSCS.

241   To determine the roles of model horizontal resolutions, tidal constituents and initial stratification in reproducing ISWs in
242   the NSCS, a set of 3D sensitivity numerical simulations are employed with different configurations, which are listed in Table
243   2. Details in configuration changes are as follows.

244   1) Exps. 3 and 4 (**250m_8HARs** and **1000m_8HARs**): Comparing to **500m_8HARs**, the horizontal resolution (Δx) is set as
245   250 m and 1000 m in both zonal and meridional directions, respectively.

246   2) Exps. 5 - 7 (**500m_1HAR**, **500m_4HARs**, and **500m_13HARs**): Comparing to **500m_8HARs**, the sensitivity experiments

247   are driven by single tidal constituent (M2), four main tidal constituents (M2, S2, K1, and O1), and thirteen tidal constituents

248   (M2, S2, N2, K2, K1, O1, P1, Q1, M4, MS4, MN4, MM, and MF), respectively.

249   3) Exp. 8 (**500m_Real_N2**): A real stratification profile of background temperature at the mooring station DS is imposed as

250   the initial condition, which is derived from the in-situ measurements. A backward-in-time low-pass filter derived from a finite

251   impulse response differential equation is used to compute the background temperature (Rayson et al., 2019).

$$\frac{d\bar{T}}{dt} = \frac{1}{\tau_f}(T - \bar{T}), \tag{5}$$

253   in which, τ_f is the filtering time scale, set to 35 h, corresponding to the local Coriolis frequency. T and $\bar{T}$ are the

254   instantaneous and background temperature, respectively. Then, the background temperature at each observational time step i

255   is given as

$$\bar{T}^{i+1} = \bar{T}^i + \frac{\Delta t}{\tau_f}(T^{i+1} - \bar{T}^i), \tag{6}$$

257   where Δt is the sampling rate (10 secs for the temperature and CTD sensors, 15 secs for the CT sensors). The background

258   temperature profile is ultimately obtained by low-pass filtering at each layer (see red line in Fig. 1b).

4.1 Requirements of resolutions

260   Various 3D model with different resolutions were implemented to simulate ISWs in the NSCS in previous studies (e.g.,

261   Vlasenko et al., 2010; Zhang et al., 2011; Lai et al., 2019). However, which resolution is adequate to satisfy the ISW prediction

262   precision and save computational resources to the utmost in the meantime has yet been discussed. Here, we run two sensitivity

263   experiments (Exps. **250m_8HARs** and **1000m_8HARs**) with horizontal resolutions of 250 m and 1000 m, to respectively

264   compare the model performance in different aspects with the control run (resolution of 500 m).

265   First, the spatial distributions of ISWs are exhibited via the snapshots of sea surface height gradients ($|\nabla \eta|$) at 12:00 UTC

266   on 12 August 2014. In the control run (**500m_8HARs**), three ISWs (labelled as IWB1, IWA1, and IWB2 from west to east)

267   with distinct crest lines successively occur between 116ºE and 120ºE (see Fig. 6a), in which IWB1 and IWB2 are internal

268   wave packets with trailing waves (type-b wave) and IWA1 is a single soliton (type-a wave). As IWB1 approaches the

269   continental slope and shelf, the leading wave front fully steepens with a narrow characteristic half-width, suggesting its strong

270   nonlinearity. IWB2 also shows up as a wave packet with many secondary waves in the developing stage, although its

271   nonlinearity is slightly weaker than IWB1's. Conversely, the single soliton IWA1 with relatively long crest line and broad

272   characteristic half-width is about to pass mooring station DS (marked as green star in Fig. 6). In comparison, the Exps.

273   **250m_8HARs** and **1000m_8HARs** reproduce these three waves as well, but with some subtle discrepancies between them. In

274   Exp. **250m_8HARs**, more details of wave properties are clarified (Fig. 6b). Specifically, the secondary waves of IWB1 and

275   IWB2 are more visible than those in **500m_8HARs**. However, in Exp. **1000m_8HARs**, some fine structures of ISWs are not

276 well resolved. For instance, only one secondary wave is found behind the leading wave of IWB2, and the south portion of
277 IWA1 crest line is barely observed (Fig. 6c).

278   Then, we select a transect along the main propagation path of ISWs (shown in dashed line in Fig. 6a) at 12:00 UTC on 12
279 August 2014 to compare the vertical structure of ISWs among three experiments (see Fig. 7). In Fig. 7, blue (yellow) color
280 shades represent westward (eastward) baroclinic velocity and contours are temperature isotherms. Linear internal waves, such
281 as internal wave beams near the generation site (120° – 121^oE), are nicely reproduced in all numerical experiments. Nonetheless,
282 nonlinear internal waves present different wave characteristics in different cases. In Exp. *500m_8HARs*, the single soliton
283 IWA1 and the wave packet IWB2 with a series of trailing waves are apparent in the slice, but IWB1 is not included (Fig. 7a).
284 In Exp. *250m_8HARs*, IWA1 and IWB2 occur at the same location as those in ***Exp. 500m_8HARs***. IWA1 show similar
285 properties in two cases, but the secondary waves of IWB2 are better described in Exp. *250m_8HARs*. By comparison, IWA1
286 shows its weak nonlinearity with small vertical displacement and broad characteristic half-width (i.e., horizontal distance
287 between the wave front and wave trough) in Exp. *1000m_8HARs*. Besides, only one secondary wave appears in the IWB2
288 packet in Exp. *1000m_8HARs*.

289   Last, a two-day time segment of observational temperature and baroclinic velocities from 18:00 UTC 11 August to 18:00
290 UTC 13 August 2014 at the station DS is extracted to demonstrate the sensitivity model capability of simulating vertical
291 structures of ISWs over the continental slope (Fig. 8). In the control run (***500m_8HARs***, Fig. 8b), two wave packets and two
292 single solitons successively arrive at the station, keeping the consistency with the observation, although their characteristic
293 half-widths are slightly broader than those in the field measurements (Fig. 8a). Meanwhile, some small fluctuations, occurring
294 in the observations, are not included in the control run. In Exp. *250m_8HARs* (Fig. 8c), the half-widths are narrower than
295 those in the Exp. *500m_8HARs*, which agree better with the real internal wave field. Besides, more fluctuations, i.e., those
296 small wave signals (09:00 UTC 12 August and 09:00 UTC 13 August) in front of the single solitons are reproduced in this
297 experiment. Conversely, in Exp. *1000m_8HARs*, internal wave trains can still be reproduced with relatively weak nonlinearity,
298 but the single solitons are not correct due to their tiny amplitudes and linear wave structures.

299   To quantitatively evaluate the model performance of sensitivity experiments, we present the bias of five wave properties of
300 fifteen ISWs (marked as red arrows in Fig. 4) between model results and observational data in Fig. 9. The biases of arrival
301 time are generally smaller than 1 h (see black and blue circles in Fig. 9a) for Exps. *500m_8HARs* and *250m_8HARs*, whose
302 RMSDs are 0.71 and 0.67 h, respectively. In contrast, the bias for Exp. *1000m_8HARs* is larger than 1 h (red circles in Fig.
303 9a) and its RMSD is 0.79 h. In terms of the wave-induced velocity (Fig. 9b), the RMSDs are 0.38, 0.41 and 0.48 m s^{-1} in Exps.
304 *250m_8HARs*, *500m_8HARs*, and *1000m_8HARs*, respectively. The RMSDs of propagation directions are very close (~8.5^o)
305 in the three experiments (see Table 3). As for the mode-1 wave amplitudes, Exps. *250m_8HARs* and *500m_8HARs*
306 overestimate the wave amplitudes in most cases (see positive biases in Fig. 9d), thereby resulting in RMSDs of 38.12 and
307 37.27 m, respectively. Conversely, Exp. *1000m_8HARs* would underestimate the wave amplitudes of majority ISWs with
308 dominant negative biases in Fig. 9d, resulting in a RMSD of 40.28 m (Table 3). Last but not least, Exps. *500m_8HARs* and
309 *1000m_8HARs* inaccurately depict characteristic half-widths of ISWs with RMSDs of 1.07 and 2.41 km, while Exp.

310 **250m_8HARs** performs well with a RMSD of 0.64 km (Fig. 9e). The relative difference of RMSD suggests that Exp.

311 **250m_8HARs** increases 40% accuracy of predicting characteristic half-widths by comparing to Exp. **500m_8HARs**. From the

312 perspective of computational resources, Exps. **250m_8HARs**, **500m_8HARs**, and **1000m_8HARs** spend 20.4×10^4 CPU

313 hours, 4.6×10^4 CPU hours, and 1.0×10^4 CPU hours, respectively.

314 In summary, the control run with a resolution of 500 m can basically reproduce the principal ISW field in the NSCS, while

315 the sensitivity model with a higher resolution of 250 m would be a better solution to identify wave properties, in particular of

316 the wave nonlinearity. Nonetheless, a 250 m-resolution model spends nearly fivefold computational resources of a 500 m-

317 resolution model in the same model domain. Besides, the model with a lower resolution of 1000 m underestimates the

318 nonlinearity of ISWs, thereby resulting in an inaccurate ISW field in the NSCS.

319 **4.2 Requirements of tidal constituents**

320 3D/2D models with different numbers of barotropic tidal constituents (e.g., single harmonic, four harmonics and eight

321 harmonics) were commonly imposed to investigate the generation mechanisms of ISWs in the NSCS in previous studies (e.g.,

322 Li, 2014; Buijsman et al., 2010; Jin et al., 2021). However, whether a single tidal constituent can satisfy the reproduction of a

323 real ISW field and how many tidal constituents are required for a realistic ISW model are still questions. Here, we run three

324 sensitivity experiments (Exps. **500m_1HAR**, **500m_4HARs** and **500m_13HARs**) with different numbers of tidal harmonics to

325 answer the questions by comparing the model performance with the control run (**500m_8HARs**).

326 We first discuss the model requirements of tidal constituents from the point of view of the ISW horizontal distributions and

327 look back to Fig. 6. Note that time series of zonal barotropic currents at the generation site (Luzon Strait) are presented on the

328 bottom left for each panel, where single/four/eight tidal constituent(s) are shown in green/magenta/blue. By comparing Exp.

329 **500m_1HAR** (Fig. 6d) and **500m_8HARs** (Fig. 6a), we find that the single M2 tidal harmonic is not adequate to reproduce

330 ISWs in the NSCS, so only some linear internal tides are detected on the sea surface via $|\nabla\eta|$. In contrast, Exp. **500m_4HARs**

331 (Fig. 6e) nearly recreates the analogous scenario of ISWs to Exp. **500m_8HARs**, where IWB1, IWA1 and IWB2 appear at the

332 same locations. Nonetheless, the crestline length (~134 km) of IWB2 in Exp. **500m_4HARs** is slightly shorter than that (~167

333 km) in Exp. **500m_8HARs**, and the secondary waves of IWB2 are unclear in Exp. **500m_4HARs** (see Fig. 6e). $|\nabla\eta|$ in Exp.

334 **500m_13HARs** are not presented in Fig. 6, since it shows the exact same spatial patterns of ISWs as those in Exp.

335 **500m_8HARs**, suggesting the principle eight tidal constituents are fine enough to satisfy accurate reproduction of the

336 horizontal features of ISWs in a realistic oceanic model.

337 We then consider the difference of ISW vertical structures in sensitivity experiments with various tidal forcing via the

338 selected transect and mooring station DS. In Exp. **500m_1HAR**, only linear internal waves are captured from the generation

339 site to the slope, suggesting that single M2 tidal constituent without amplification factors can only contributes to internal tides

340 and linear internal wave beams in NSCS (see Figs. 7d and 8e), unless the magnitudes of M2 barotropic tides are amplified,

341 ISWs are likely to be generated (e.g., Yuan et al., 2020). In Exp. **500m_4HARs** (Figs. 7e and 8f), the single soliton IWA1 is

342 reproduced with a smaller amplitude and weaker nonlinearity than that in Exp. **500m_8HARs**. Besides, the secondary waves

343 of IWB2 are barely observed in Exp. ***500m_4HARs***, which are much clearer in Exp. ***500m_8HARs*** (Figs. 7a and 8a). Figs. 8a

344 and 8g depict the striking similarity of wave characteristics between Exp. ***500m_8HARs*** and Exp. ***500m_13HARs***.

345 Last, we quantitatively estimate the sensitivity model capability of reproducing ISWs, by computing the biases and RMSDs

346 of five wave properties (see Fig. 9 and Table 3) in the cases with different tidal forcing. Since Exp. ***500m_1HAR*** cannot predict

347 ISWs with significant amplitudes, we exclude it in the following analysis. In terms of Exp. ***500m_13HARs*** with thirteen tidal

348 constituents, the biases and RMSDs of five wave properties are very close to those in the control run with eight harmonics (see

349 overlapped black circles and magenta triangles in Fig. 9 and Table 3). Conversely, Exp. ***500m_4HARs*** shows significant

350 difference in the biases and RMSDs of five wave properties from the control run. Specifically, in Fig. 9a, the RMSD of arrival

351 time (0.81 h) is larger in Exp. ***500m_4HARs*** than that in Exp. ***500m_8HARs*** (0.71 h). In addition, Exp. ***500m_4HARs***

352 underestimates averaged wave-induced velocity for about 38% and averaged mode-1 wave amplitude for about 15%, which

353 result in large negative values of biases (see magenta triangles in Figs. 9b and 9c), corresponding to 0.58 m s^{-1} and 43.69 m of

354 RMSDs, respectively. In terms of the characteristic half-widths, Exps. ***500m_4HARs*** and ***500m_13HARs*** with RMSDs of

355 1.10 and 1.01 km show analogous performance to the control run Exp. ***500m_8HARs*** with a RMSD of 1.07 km.

356 In summary, the model with eight (or thirteen) primary tidal constituents can accurately reproduce the real ISW field in the

357 NSCS, while the sensitivity model with four key harmonics (M2, S2, K1 and O1) would underestimate the magnitudes of

358 some secondary wave within a wave packet. In addition, the model only driven by M2 tide can only characterize wave

359 properties of linear internal waves (tides) instead of ISWs.

4.3 Initial stratification selections

361 As ISWs generate via tide-topography interaction in the stratified water, the stratification selection is crucial to directly

362 affect the model capabilities. Here, we extract the background stratification from the in-situ measurements at mooring station

363 DS as initial condition to run the sensitivity experiment ***500m_Real_N2***, and compare the model results with the control run

364 (***500m_8HARs***) with a climatological stratification from the WOA18 dataset.

365 In the model results, the spatial distribution of $|\nabla\eta|$ in Exp. ***500m_Real_N2*** shows analogous pattern of ISWs to that in Exp.

366 ***500m_8HARs***. Specifically, three ISWs (i.e., IWB1, IWA1, and IWB2) appear at the same location in the two experiments

367 with similar horizontal wave characteristics (Figs. 6a and 6f). The visible difference is that the crest line length of the secondary

368 wave of IWB2 is longer with a stronger nonlinearity in Exp. ***500m_Real_N2***. We then look over the difference of ISW vertical

369 structures between two cases from the perspective of *x-z* plane along the transect (Figs. 7a and 7f) and time series at station

370 DS (Figs. 8a and 8h). It is clearly shown that Exp. ***500m_Real_N2*** with the real stratification can better characterize the

371 nonlinearity of the single soliton IWA1 and the secondary wave of wave train IWB2. Besides, the comparison with field

372 measurements reveals that Exp. ***500m_Real_N2*** shows a better precision (13%) in predicting the arrival time (i.e., RMSD of

373 0.62 h) of ISWs than the control run (i.e., RMSD of 0.71 h) with the climatological stratification. However, the RMSD of the

374 propagation direction of ISWs is larger in the realistic-stratification case (14.74°) than that of the control run (8.35°). Last, Exp.

375 ***500m_Real_N2*** nicely describes the characteristic half-widths of ISWs (RMSD of 0.58 km), which improves 46% accuracy

by comparing that in Exp. ***500m_8HARs*** (RMSD of 1.07 km). To sum up, although the model with climatological stratification works well, applying the real background stratification as the model initial condition would improve the model performance in predicting some wave properties, including arrival time, wave-induced velocity, wave amplitude and characteristic half-width.

5 Discussion and Conclusions

Although the 3D realistic model, particularly in Exp. ***250m_8HARs***, has accurately reproduced the ISW features in the NSCS to some extent, the depictions of soliton numbers within an internal wave packet and propagation direction still have space for improvement, i.e., at least three following factors might be considered in the future modelling.

The first factor, that may affect the model accuracy, is background currents. Here, we download the global Hybrid Coordinate Ocean Model (HYCOM) dataset in 2014 and calculate the background current field by averaging from 05-AUG to 20-AUG, namely predicting time of the model (see Fig. 10a). In Fig. 10a, there is a clear counter-clockwise circulation/eddy pattern on the west side of Luzon Strait. Xie et al. (2015) suggested that wave properties of ISWs can be significantly influenced by an isolated mesoscale eddy, regardless of a cyclonic or anticyclonic eddy, during the propagation of ISWs. When an ISW pass over a cyclonic eddy, as in Fig. 10a, the crestline will be distorted, thereby modulating the oblique propagation direction of wave to some extent (Xie et al., 2016). In addition, a series of secondary trailing waves are able to form behind the leading wave in the energy-focusing region. Therefore, background currents are supposed to be considered in the future forecasting model, which shows potential improvement in the depiction of soliton numbers within an ISW packet and propagation direction in the NSCS.

The second factor is inhomogeneous spatial distribution of stratification. In the current forecasting model, we apply horizontally-homogeneous temperature and salinity profiles (Fig. 1d) with the maximum buoyancy frequency of ~0.02 s^{-1} at a water depth of 50 m. Actually, we also implement a sensitivity experiment (EXP. ***3D-TS***) with weak spatially-varying initial conditions derived from the WOA18 climatology dataset. By comparing EXPs. ***3D-TS*** and ***800m_HARs***, it is concluded that the weak spatially-varying initial conditions show similar performance in predicting the arrival time and horizontal distributions (Fig. C1), wave amplitudes and wave-induced velocities (Fig. C2) of ISWs to the horizontally-homogeneous initial conditions. However, the model results would be different with strong spatially-varying stratification derived from the ocean reanalysis dataset with a high resolution and sampling rate (e.g., global HYCOM dataset). Since wave speeds of ISWs and internal tides are closely related to vertical structure of stratification based on eigen-function, the inhomogeneous stratification pattern is likely to affect ISW propagation speed and then modulate their arrival time. Most of previous numerical studies (e.g., Zhang et al., 2011; Alford et al., 2015; Zeng et al., 2019) rarely considered the impacts of horizontally inhomogeneous stratification, but Chi et al. (2016) and Lai et al. (2019) applied spatially-varying stratification in 3D model and indicated that inhomogeneous stratification can achieve better model results to some extent. However, only considering spatially-varying temperature and salinity profiles with large values of horizontal gradients (e.g., HYCOM dataset in Fig. 10b)

408 as the initial conditions might lead to spurious geostrophic currents, thereby significantly affecting the true wave field. Hence,

409 spatially-varying stratification is worthwhile to be considered together with background currents in future numerical studies

410 in the NSCS.

411   The last element is external (wind) forcing. As is well known, ISWs are a ubiquitous phenomenon with maximum amplitudes

412 in the ocean interior. Nonetheless, the thermoclines usually occur in the upper layers (shallower than 500 m) in the SCS, which

413 can be significantly affected by extreme wind events (i.e., tropical cyclones, Zhang 2022). So far, wind forcing was rarely

414 applied in the numerical modelling of ISWs, except Lai et al. (2019). As both the ISWs and tropical cyclones are active and

415 frequent in August, September and October in the SCS, the impacts of tropical cyclones on the upper layers should be

416 considered in the future numerical simulations, although tropical cyclone did not happen during our predicting period (see Fig.

417 10c).

418   In summary, this study introduces a robust ISW forecasting model by comparing with in-situ observational data and remote-

419 sensing images, and quantitatively evaluates the requirements of different factors, including the horizontal resolutions, tidal

420 constituents and initial stratification, for accurately characterizing the ISW field with applications to the NSCS. The major

421 findings are listed as follows.

422   1)   A model with a 500 m resolution can basically reproduce the principal ISW field, while a model with a higher resolution

423   of 250 m would be a better solution to identify wave properties but spends nearly fivefold computational resources of

424   a 500 m-resolution case with the same model domain.

425   2)   At least eight primary tidal constituents should be included in the boundary forcing.

426   3)   Compared to climatological stratification, applying the observational background stratification could improve the

427   model performance in predicting some wave properties, namely 13% improvement of arrival time and 46%

428   improvement of characteristic half-width.

429 **Appendix A: Feasibility study of 2D slice model**

430   Differing from the 3D models, 2D slice models are fairly economical from the perspective of computational resources. In

431 the past few decades, 2D slice models with idealized topography (double ridges) were commonly conducted to investigate

432 ISW dynamics in the NSCS, in particular for the generation mechanisms and the affecting factors of ISWs (i.e., Cai et al.,

433 2002; Shaw et al., 2009; Li, 2014). Here, we attempt to test the 2D model performance along different transects and clarify

434 whether a 2D slice model can be a substitute for a 3D model in the aspect of reproducing a real ISW field in the NSCS.

435   Three parallel transects with a distance of 0.05° are selected along the main propagation direction of ISWs (see dashed lines

436 in Fig. 1a), which are labelled as *2D_500m_8HARs*, *2D_500m_8HARs_005N*, and *2D_500m_8HARs_005S*. Δx and Δt are

437 still set as 500 m and 10 sec, respectively. Initial conditions and dissipation coefficients are set the same as those in the 3D

438 control run (*500m_8HARs*). The 2D slice models are also driven by the barotropic tides of eight tidal constituents at both west

439 boundary (115.8°E, 21.1°N $\pm$ 0.05°) and east boundary (123.8°E, 19.5°N $\pm$ 0.05°). As the transects are not strictly zonal (angle

440    $\theta = 11.2°$, see Fig. 1a), it is necessary to extract the amplitude (U') and phase (ϕ') for each harmonic (ω) in the transect

441   direction from the TPXO8-atlas dataset (i.e., U, V, ϕ_U, and ϕ_V), given by

442

$$U' = \sqrt{(U \cdot cos\phi_U cos\theta - V \cdot cos\phi_V sin\theta)^2 + (U \cdot sin\phi_U cos\theta - V \cdot sin\phi_V sin\theta)^2}, \quad (A1)$$

$$\phi' = arctan\left(\frac{U \cdot sin\phi_U cos\theta - V \cdot sin\phi_V sin\theta}{U \cdot cos\phi_U cos\theta - V \cdot cos\phi_V sin\theta}\right), \quad (A2)$$

445   Here, we apply the standard 2D experiment along the selected transect (see the black dashed line in Fig. 1a) and label it as

446   ***2D_500m_8HARs***. The model is driven by eight principle tidal constituents on the both lateral boundaries, which are extracted

447   from the TPXO8 dataset (following Eqns. A1 and A2). Note that initial conditions and other model configurations in Exp.

448   ***2D_500m_8HARs*** are the same as those in the 3D control run (***500m_8HARs***). In addition, we run two sensitivity experiments

449   (Exps. ***2D_500m_8HARs_005N*** and ***2D_500m_8HARs_005S***) along the two parallel transects (see red dashed lines in Fig.

450   1b).

451   In the 2D standard case (***2D_500m_8HARs***), ISWs subsequently generate in the double ridge, then propagate westward,

452   and eventually arrive at the station in the form of wave trains (Fig. A1b). The wave amplitudes are greater than those in the

453   3D control run (Fig. A1a). At the station outputs (Fig. A1f), we find that Exp. ***2D_500m_8HARs*** can only reproduce ISW

454   packets, but cannot discriminate type-a and type-b ISWs. Although the occurrence frequency of ISWs is also twice per day in

455   Exp. ***2D_500m_8HARs***, the arrival time of those ISW packets is not consistent with that in Exp. ***500m_8HARs*** (Fig. A1e) and

456   in the field measurements (Fig. 8a). In Exp. ***2D_500m_8HARs_005N***, ISWs are rarely found along the transect (Fig. A1c),

457   likely due to the relatively gentle topography and small tidal forcing at the lateral boundaries. At the station outputs (Fig. A1g),

458   only small temperature fluctuations are captured. Conversely, Exp. ***2D_500m_8HARs_005S*** show analogous wave fields to

459   Exp. ***2D_500m_8HARs*** (Fig. A1d). Specifically, ISW packets with a half-day cycle are dominant, but their arrival time are

460   postponed for about two hours (Fig. A1h).

461   To sum up, 2D slice models along different transects (even 0.05° apart) present totally different ISW characteristics, which

462   are inconsistent with the 3D model results and in-situ measurements. Therefore, 3D model is the best and sole option to

463   correctly reproduce the ISW field in the real ocean, while 2D model is more suitable for the mechanism investigations.

464   **Appendix B: Quasi-steady state of the model**

465   Due to the limitation of the computational resources, we admit that the model integrated time (3-day) might be relatively

466   short for the model spin-up. When we calculate the averaged baroclinic kinetic energy (KE_{bc}) in the inner model domain (Fig.

467   B1), it is found that the depth-integrated KE_{bc} keeps increasing in the first 7 days (see red line in Fig. B1a), which is related

468   to the flooding barotropic tides (see Fig. B1b). Actually, $\int_{-H}^{0} KE_{bc}\, dz$ reaches 10 kJ m^{-2} in the 3rd model day, whose magnitude

469   is equivalent to that during the neap tides (i.e., 12th to 15th model day). It demonstrates that the 3D model reaches a quasi-

470   steady state after three days. Moreover, the comparison between the model results and field observations at the mooring station

471 DS verifies the model accuracy since 08 August (the 3rd model day) as well. Therefore, first 3 days are considered as the spin-
472 up time in this work.

473 **Appendix C: Figures of EXPs.** *3D-TS* and *500m_8HARs*

474

475 *Code and data availability*. The MODIS remote-sensing images are derived from the NASA Worldview application
476 (https://worldview.earthdata.nasa.gov). The input files (including initial and boundary conditions) and relevant output data
477 files of the 3D realistic Massachusetts Institute of Technology general circulation model in the northern South China Sea are
478 available at a free, open access, data repository via https://doi.org/10.5281/zenodo.6792999.

479

480 *Author contributions*. YG wrote the paper with the help of all the co-authors. XC, JX, JX, ZC, YH and SC provided constructive
481 feedback on the manuscript. JX gave help and advice in observational data processing and numerical simulations.

482

483 *Competing interests*. The authors declare that they have no conflict of interest.

484

485 *Financial support*. This work was jointly supported by the National Natural Science Foundation of China (NSFC) under
486 contract Nos. 42130404, 91858201, 42206012, 42276015, 42276022 and 42176025; the Key Research Program of Frontier
487 Sciences, Chinese Academy of Sciences (CAS) under contract No. QYZDJ-SSW-DQC034; Grant No. GML2019ZD0304
488 from Southern Marine Science and Engineering Guangdong Laboratory (Guangzhou); the China Postdoctoral Science
489 Foundation (2022M713232); Grant No. ISEE2021PY01 from CAS; Youth science and technology innovation talent of
490 Guangdong TeZhi plan (2019TQ05H519); Rising Star Foundation of SCSIO (NHXX2019WL0201); Natural Science
491 Foundation of Guangdong Province (2020A1515010495, 2021A1515012538, 2021A1515011613); the Youth Innovation
492 Promotion Association from CAS (2019336); the State Key Laboratory of Tropical Oceanography Independent Research
493 Program under contract No. LTOZZ2205. The numerical simulation is supported by the High Performance Computing
494 Division and HPC managers of Wei Zhou and Dandan Sui in the South China Sea Institute of Oceanology.

495

496 **References**

497 Alford, M. H., MacKinnon, J. A., Nash, J. D., Simmons, H., Pickering, A., Klymak, J. M., Pinkel, R., Sun, O., Rainville, L.,
498 Musgrave, R., Beitzel, T., Fu, K. H., and Lu, C. W.: Energy flux and dissipation in Luzon Strait: Two tales of two
499 ridges. Journal of Physical Oceanography, 41, 2211-2222, https://doi.org/10.1175/JPO-D-11-073.1, 2011.

500 Alford, M. H., Peacock, T., MacKinnon, J. A., Nash, J. D., Buijsman, M. C., Centurioni, L. R., ... and Paluszkiewicz, T.: The
501 formation and fate of internal waves in the South China Sea, Nature, 521, 65-69, https://doi.org/10.1038/nature14399, 2015.

502 Álvarez, Ó., Izquierdo, A., González, C. J., Bruno, M., and Mañanes, R.: Some considerations about non-hydrostatic vs.
503 hydrostatic simulation of short-period internal waves. A case study: The Strait of Gibraltar. Continental Shelf Research, 181,
504 174-186, https://doi.org/10.1016/j.csr.2019.05.016, 2019.

505 Beardsley, R. C., Duda, T. F., Lynch, J. F., Irish, J. D., Ramp, S. R., Chiu, C. S., Tang, T. Y., Yang, Y. J., and Fang, G.:
506 Barotropic tide in the northeast South China Sea, IEEE Journal of Oceanic Engineering, 29, 1075-1086,
507 https://doi.org/10.1109/JOE.2004.833226, 2004.

508 Buijsman, M. C., Kanarska, Y., and McWilliams, J. C.: On the generation and evolution of nonlinear internal waves in the
509 South China Sea, Journal of Geophysical Research: Oceans, 115, https://doi.org/10.1029/2009JC005275, 2010.

510 Buijsman, M. C., McWilliams, J. C., and Jackson, C. R.: East-west asymmetry in nonlinear internal waves from Luzon
511 Strait, Journal of Geophysical Research: Oceans, 115, https://doi.org/10.1029/2009JC006004, 2010.

512 Cai, S., Long, X., and Gan, Z.: A numerical study of the generation and propagation of internal solitary waves in the Luzon
513 Strait, Oceanologica Acta, 25, 51-60, https://doi.org/10.1016/S0399-1784(02)01181-7, 2002.

514 Chen, Z., Nie, Y., Xie, J., Xu, J., He, Y., and Cai, S.: Generation of internal solitary waves over a large sill: From Knight Inlet
515 to Luzon Strait, Journal of Geophysical Research: Oceans, 122, 1555-1573, https://doi.org/10.1002/2016JC012206, 2017.

516 Cummins, P. F., and Oey, L. Y.: Simulation of barotropic and baroclinic tides off northern British Columbia, Journal of
517 Physical oceanography, 27, 762-781, https://doi.org/10.1175/1520-0485(1997)027<0762:SOBABT>2.0.CO;2, 1997.

518 Du, T., Tseng, Y. H., and Yan, X. H.: Impacts of tidal currents and Kuroshio intrusion on the generation of nonlinear internal
519 waves in Luzon Strait, Journal of Geophysical Research: Oceans, 113, https://doi.org/10.1029/2007JC004294, 2008.

520 Egbert, G. D., and Erofeeva, S. Y.: Efficient inverse modeling of barotropic ocean tides, Journal of Atmospheric and Oceanic
521 technology, 19, 183-204, https://doi.org/10.1175/1520-0426(2002)019<0183:EIMOBO>2.0.CO;2, 2002.

522 Farmer, D., Li, Q., and Park, J. H.: Internal wave observations in the South China Sea: The role of rotation and non-
523 linearity, Atmosphere-Ocean, 47, 267-280, https://doi.org/10.3137/OC313.2009, 2009.

524 Farmer, D. M., Alford, M. H., Lien, R. C., Yang, Y. J., Chang, M. H., and Li, Q.: From Luzon Strait to Dongsha Plateau:
525 Stages in the life of an internal wave, Oceanography, 24, 64-77, 2011.

526 Gerkema, T., and Zimmerman, J. T. F.: An introduction to internal waves, Lecture Notes, Royal NIOZ, Texel, 207, 2008.

527 Guo, C., Chen, X., Vlasenko, V., and Stashchuk, N.: Numerical investigation of internal solitary waves from the Luzon Strait:
528 Generation process, mechanism and three-dimensional effects, Ocean Modelling, 38, 203-216,
529 https://doi.org/10.1016/j.ocemod.2011.03.002, 2011.

530 Huang, W., Johannessen, J., Alpers, W., Yang, J., and Gan, X.: Spatial and temporal variations of internal wave sea surface
531 signatures in the northern South China Sea studied by spaceborne SAR imagery, In Proceedings of the 2nd SeaSAR
532 Symposium, 2008.

Jan, S., Lien, R. C., and Ting, C. H.: Numerical study of baroclinic tides in Luzon Strait. Journal of Oceanography, 64, 789-802, https://doi.org/10.1007/s10872-008-0066-5, 2008.

Jin, G., Lai, Z., and Shang, X.: Numerical study on the spatial and temporal characteristics of nonlinear internal wave energy in the Northern South China sea, Deep Sea Research Part I: Oceanographic Research Papers, 178, 103640, https://doi.org/10.1016/j.dsr.2021.103640, 2021.

Ko, D. S., Martin, P. J., Rowley, C. D., and Preller, R. H.: A real-time coastal ocean prediction experiment for MREA04. Journal of Marine Systems, 69, 17-28, https://doi.org/10.1016/j.jmarsys.2007.02.022, 2008.

Lai, Z., Jin, G., Huang, Y., Chen, H., Shang, X., and Xiong, X.: The generation of nonlinear internal waves in the South China Sea: A three-dimensional, nonhydrostatic numerical study, Journal of Geophysical Research: Oceans, 124, 8949-8968, https://doi.org/10.1029/2019JC015283, 2019.

Legg, S., and Huijts, K. M.: Preliminary simulations of internal waves and mixing generated by finite amplitude tidal flow over isolated topography, Deep Sea Research Part II: Topical Studies in Oceanography, 53, 140-156, https://doi.org/10.1016/j.dsr2.2005.09.014, 2006.

Li, Q.: Numerical assessment of factors affecting nonlinear internal waves in the South China Sea, Progress in Oceanography, 121, 24-43, https://doi.org/10.1016/j.pocean.2013.03.006, 2014.

Li, D., Chen, X., and Liu, A.: On the generation and evolution of internal solitary waves in the northwestern South China Sea, Ocean Modelling, 40, 105-119, https://doi.org/10.1016/j.ocemod.2011.08.005, 2011.

Liu, A. K., Chang, Y. S., Hsu, M. K., and Liang, N. K.: Evolution of nonlinear internal waves in the East and South China Seas, Journal of Geophysical Research: Oceans, 103, 7995-8008, https://doi.org/10.1029/97JC01918, 1998.

Liu, A. K., and Hsu, M. K.: Internal wave study in the South China Sea using synthetic aperture radar (SAR), International Journal of Remote Sensing, 25, 1261-1264, https://doi.org/10.1080/01431160310001592148, 2004.

Locarnini, M. M., Mishonov, A. V., Baranova, O. K., Boyer, T. P., Zweng, M. M., Garcia, H. E., Reagan, J. R., Seidov, D., Weathers, K. W., Paver, C. R., and Smolyar, I.: World ocean atlas 2018, volume 1: Temperature, 2018.

Marshall, J., Hill, C., Perelman, L., and Adcroft, A.: Hydrostatic, quasi-hydrostatic, and nonhydrostatic ocean modelling, Journal of Geophysical Research: Oceans, 102, 5733-5752, https://doi.org/10.1029/96JC02776, 1997.

Orr, M. H., and Mignerey, P. C.: Nonlinear internal waves in the South China Sea: Observation of the conversion of depression internal waves to elevation internal waves, Journal of Geophysical Research: Oceans, 108, https://doi.org/10.1029/2001JC001163, 2003.

Nagai, T., and Hibiya, T.: Internal tides and associated vertical mixing in the Indonesian Archipelago. Journal of Geophysical Research: Oceans, 120, 3373-3390, https://doi.org/10.1002/2014JC010592, 2015.

Ramp, S. R., Tang, T. Y., Duda, T. F., Lynch, J. F., Liu, A. K., Chiu, C. S., Bahr, F., L., Kim, H., R., and Yang, Y. J.: Internal solitons in the northeastern South China Sea, Part I: Sources and deep water propagation. IEEE Journal of Oceanic Engineering, 29, 1157-1181, 2004.

Ramp, S. R., Park, J. H., Yang, Y. J., Bahr, F. L., and Jeon, C.: Latitudinal structure of solitons in the South China Sea, Journal of Physical Oceanography, 49, 1747-1767, https://doi.org/10.1175/JPO-D-18-0071.1, 2019.

Rayson, M. D., Jones, N. L., and Ivey, G. N.: Temporal variability of the standing internal tide in the Browse Basin, Western Australia, Journal of Geophysical Research: Oceans, 117, https://doi.org/10.1029/2011JC007523, 2012.

Rayson, M. D., Jones, N. L., and Ivey, G. N.: Observations of large-amplitude mode-2 nonlinear internal waves on the Australian North West shelf, Journal of Physical Oceanography, 49, 309-328, https://doi.org/10.1175/JPO-D-18-0097.1, 2019.

Simmons, H., Chang, M. H., Chang, Y. T., Chao, S. Y., Fringer, O., Jackson, C. R., and Ko, D. S.: Modeling and prediction of internal waves in the South China Sea, Oceanography, 24, 88-99, 2011.

Shaw, P. T., Ko, D. S., and Chao, S. Y.: Internal solitary waves induced by flow over a ridge: With applications to the northern South China Sea, Journal of Geophysical Research: Oceans, 114, https://doi.org/10.1029/2008JC005007, 2009.

Stewart, K. D., Hogg, A. M., Griffies, S. M., Heerdegen, A. P., Ward, M. L., Spence, P., and England, M. H.: Vertical resolution of baroclinic modes in global ocean models, Ocean Modelling, 113, 50-65, https://doi.org/10.1016/j.ocemod.2017.03.012, 2017.

Thompson, D. R., and Gasparovic, R. F.: Intensity modulation in SAR images of internal waves, Nature, 320, 345-348, https://doi.org/10.1038/320345a0, 1986.

Jackson, C. R., Da Silva, J. C., and Jeans, G.: The generation of nonlinear internal waves, Oceanography, 25, 108-123, 2012.

Vlasenko, V., Stashchuk, N., Guo, C. H. U. N. S. H. E. N. G., and Chen, X.: Multimodal structure of baroclinic tides in the South China Sea, Nonlinear Processes in Geophysics, 17, 529-543, https://doi.org/10.5194/npg-17-529-2010, 2010.

Xu, J., He, Y., Chen, Z., Zhan, H., Wu, Y., Xie, J., Shang, X., Ning, D., Fang, W., and Cai, S.: Observations of different effects of an anti-cyclonic eddy on internal solitary waves in the South China Sea, Progress in Oceanography, 188, 102422, https://doi.org/10.1016/j.pocean.2020.102422, 2020.

Zeng, Z., Chen, X., Yuan, C., Tang, S., and Chi, L.: A numerical study of generation and propagation of type-a and type-b internal solitary waves in the northern South China Sea, Acta Oceanologica Sinica, 38, 20-30, https://doi.org/10.1007/s13131-019-1495-2, 2019.

Zhang, Z., Fringer, O. B., and Ramp, S. R.: Three-dimensional, nonhydrostatic numerical simulation of nonlinear internal wave generation and propagation in the South China Sea, Journal of Geophysical Research: Oceans, 116, https://doi.org/10.1029/2010JC006424, 2011.

Zhang, H.: Modulation of Upper Ocean Vertical Temperature Structure and Heat Content by a Fast-Moving Tropical Cyclone. Journal of Physical Oceanography, https://doi.org/10.1175/JPO-D-22-0132.1, 2022.

Zhao, Z., Klemas, V., Zheng, Q., and Yan, X. H.: Remote sensing evidence for baroclinic tide origin of internal solitary waves in the northeastern South China Sea, Geophysical research letters, 31, https://doi.org/10.1029/2003GL019077, 2004.

Zhao, Z., and Alford, M. H.: Source and propagation of internal solitary waves in the northeastern South China Sea, Journal of Geophysical Research: Oceans, 111, https://doi.org/10.1029/2006JC003644, 2006.

599 Zheng, Q., Yuan, Y., Klemas, V., and Yan, X. H.: Theoretical expression for an ocean internal soliton synthetic aperture radar
600 image and determination of the soliton characteristic half width, Journal of Geophysical Research: Oceans, 106, 31415-31423,
601 https://doi.org/10.1029/2000JC000726, 2001.

602 Zheng, Q., Susanto, R. D., Ho, C. R., Song, Y. T., and Xu, Q.: Statistical and dynamical analyses of generation mechanisms
603 of solitary internal waves in the northern South China Sea, Journal of Geophysical Research: Oceans, 112,
604 https://doi.org/10.1029/2006JC003551, 2007.

605

606
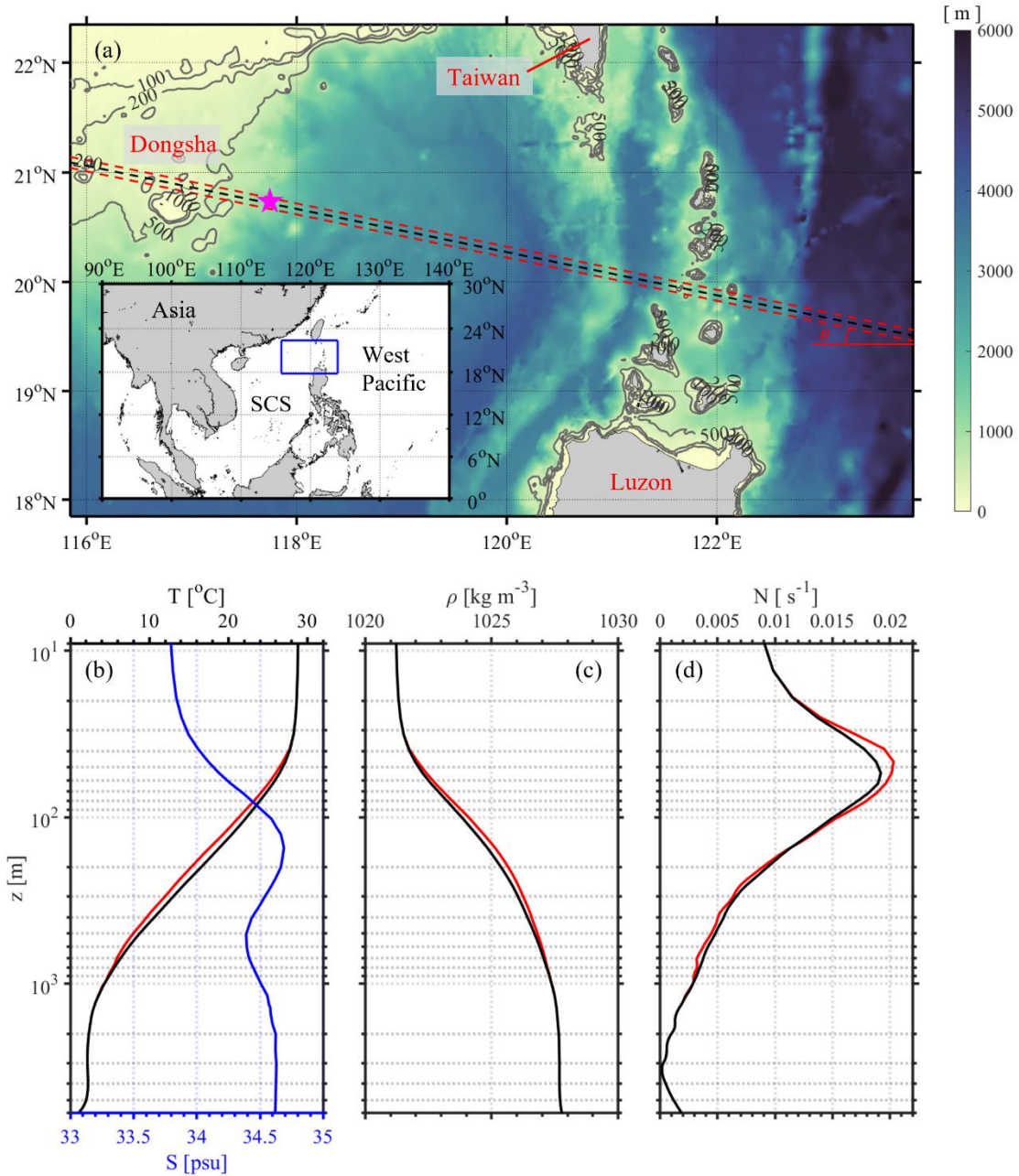
Figure 1. (a) Bathymetry map of model domain in the northern South China Sea with a mooring station DS (marked as magenta star) in the vicinity of Dongsha Atoll and the transects in 2D models, among which Exp. *2D_500m_8HARs* is in black dashed line while Exps. *2D_500m_8HARs_005N* and *2D_500m_8HARs_005S* are in red dashed lines. (b) Initial temperature and salinity profiles. (c) Density profile. (d) Buoyancy frequency profile. Note the black and red lines in (b-d) represent the data derived from the WOA18 and in-situ observations, respectively.
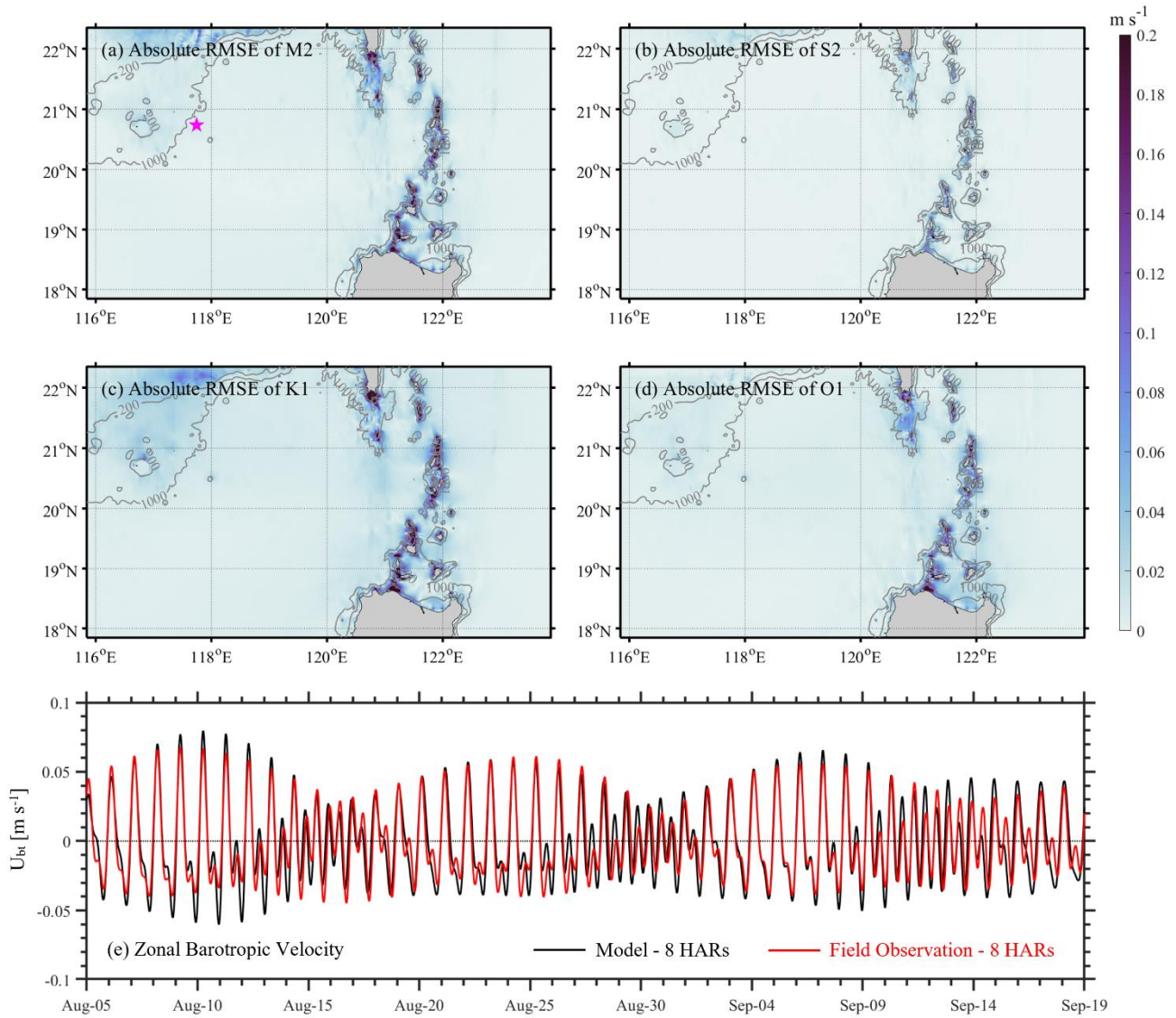
Figure 2. Absolute root-mean-square errors of zonal barotropic velocity (U_{bt}) between the model (500m_8HARs_BT) and the TPXO8-Atlas dataset for M2 (a), S2 (b), K1 (c), and O1 (d). (e) Reconstructed time series of zonal barotropic velocity at station DS (marked as magenta star in Fig. 2a) of Exp. *500m_8HARs_BT* (black line) versus measured data (red line) obtained by eight key tidal constituents.

615
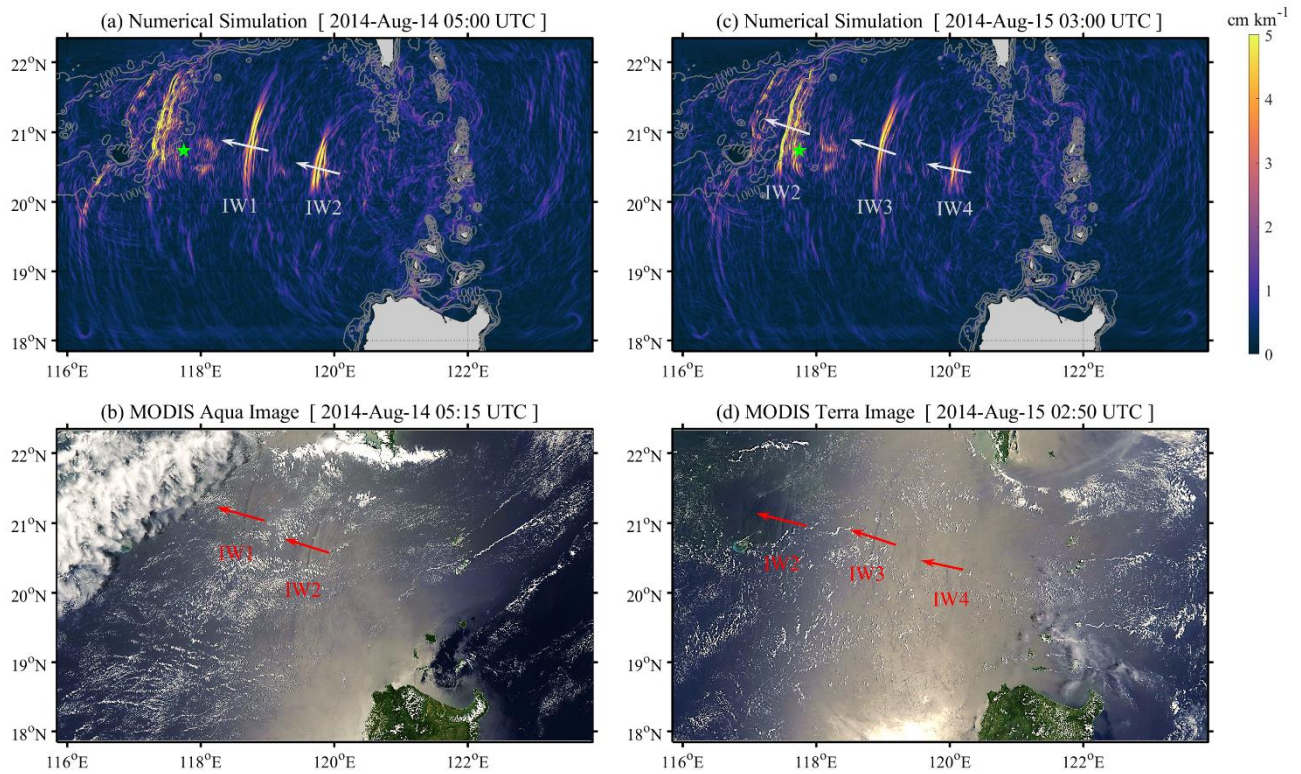
Figure 3. (a) Sea surface height gradients induced by internal solitary waves (ISWs) at 05:00 UTC on 14 August 2014 and (b)
MODIS-Aqua image obtained at 05:15 UTC on 14 August 2014. (c) Same as (a) but at 03:00 UTC on 15 August 2014. (d)
Same as (b) but for MODIS-Terra at 02:50 UTC on 15 August 2014. Note that the MODIS images in (b) and (d) are freely
downloaded from the NASA Worldview application (https://worldview.earthdata.nasa.gov, open source).
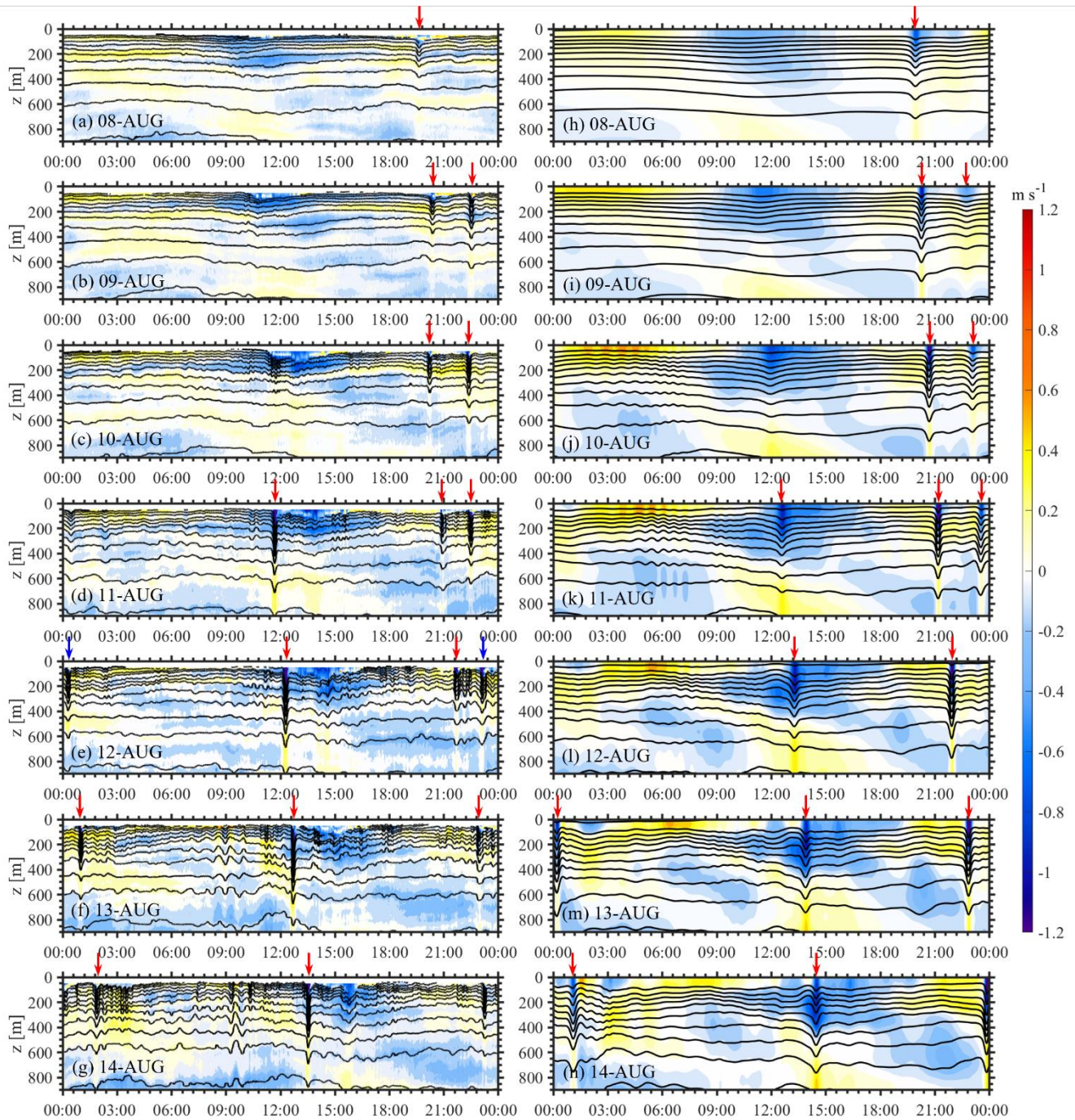
Figure 4. (a - g) Temperature isotherms (contours) and baroclinic velocities (shades) in the wave propagation direction from 08 August to 14 August at station DS from in-situ observation. (h – n) Same as (a – g) but for the model (***500m_8HARs***). Red arrows indicate ISWs that model captured, while blue arrows present the missed ones.
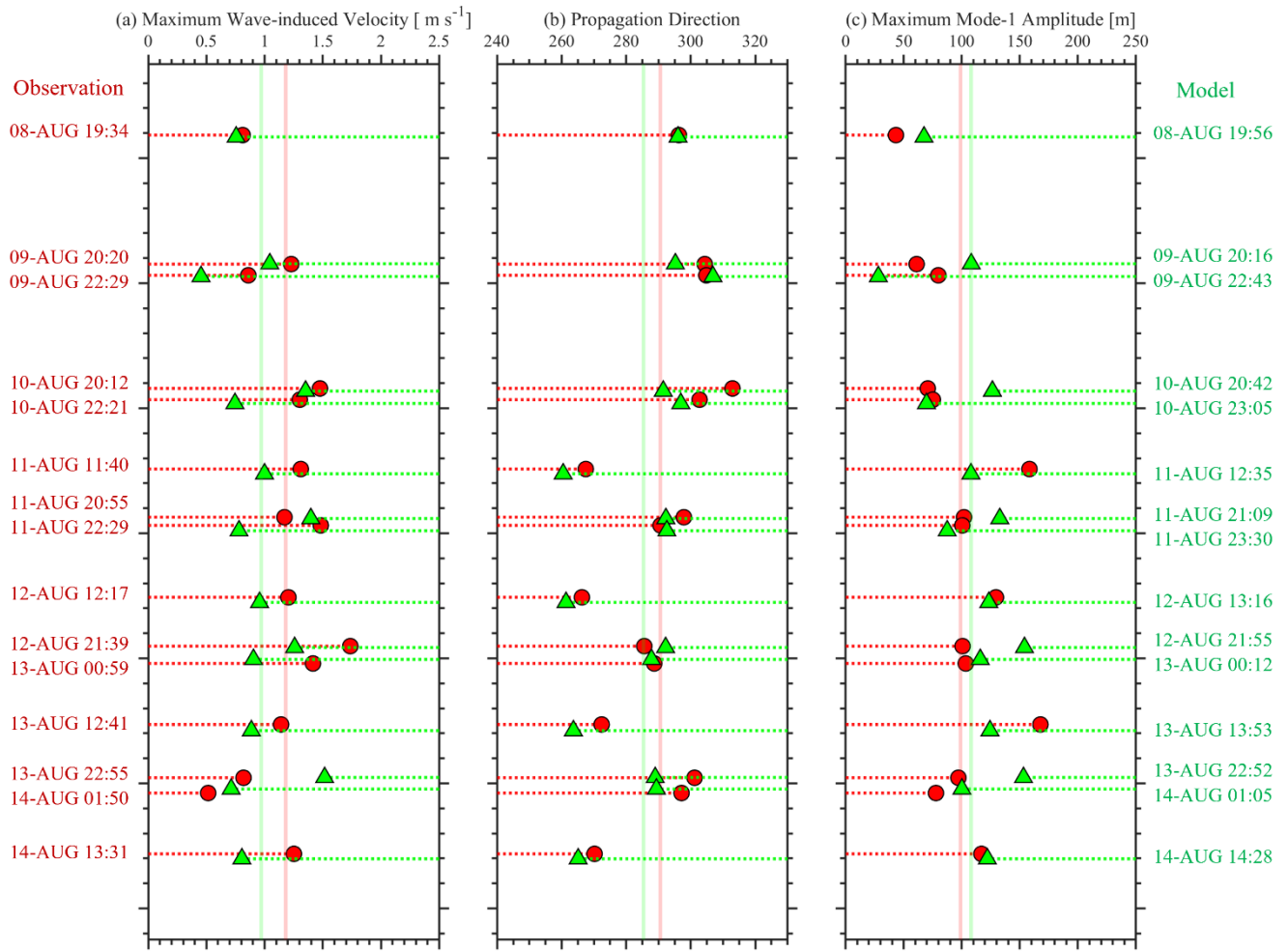
Figure 5. Maximum wave-induced velocities (a), propagation directions (b) and maximum mode-1 wave amplitudes (c) of fifteen ISWs at station DS from in-situ observations (red circles) and numerical models (green triangles). Averaged values are shown by solid lines.
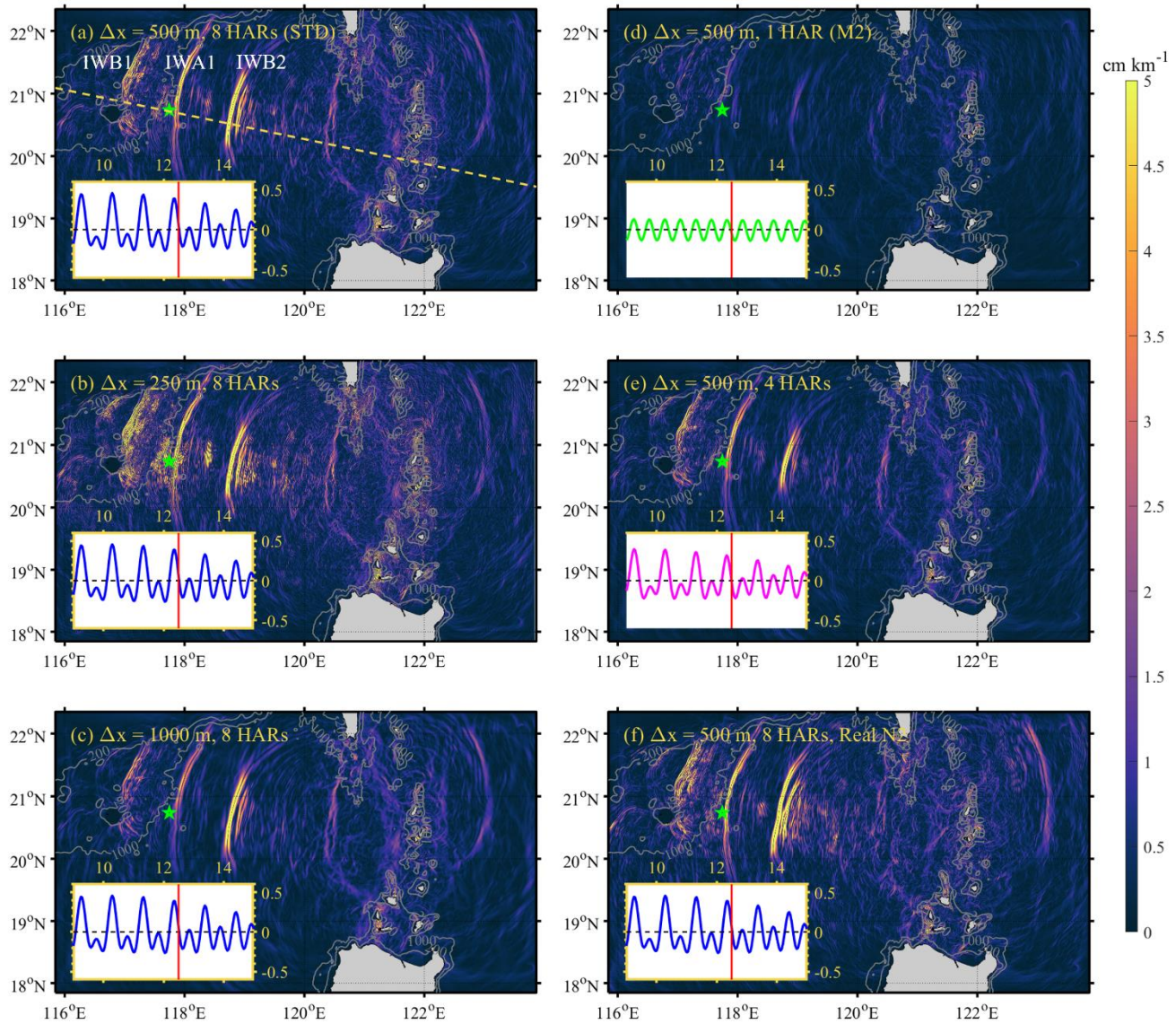
Figure 6. Sea surface height gradients at 12:00 UTC on 12 August 2014 in the model (a) ***500m_8HARs***, (b) ***250m_8HARs***, (c) ***1000m_8HARs***, (d) ***500m_1HAR***, (e) ***500m_4HARs***, and (f) ***500m_Real_N2***. Note that dashed line in (a) is selected transect to present vertical structure of ISWs. Small panels on the bottom left indicate the zonal barotropic velocity (unit in m s^{-1}) in the Luzon Strait with the solid lines showing the tidal conditions at the selected time.
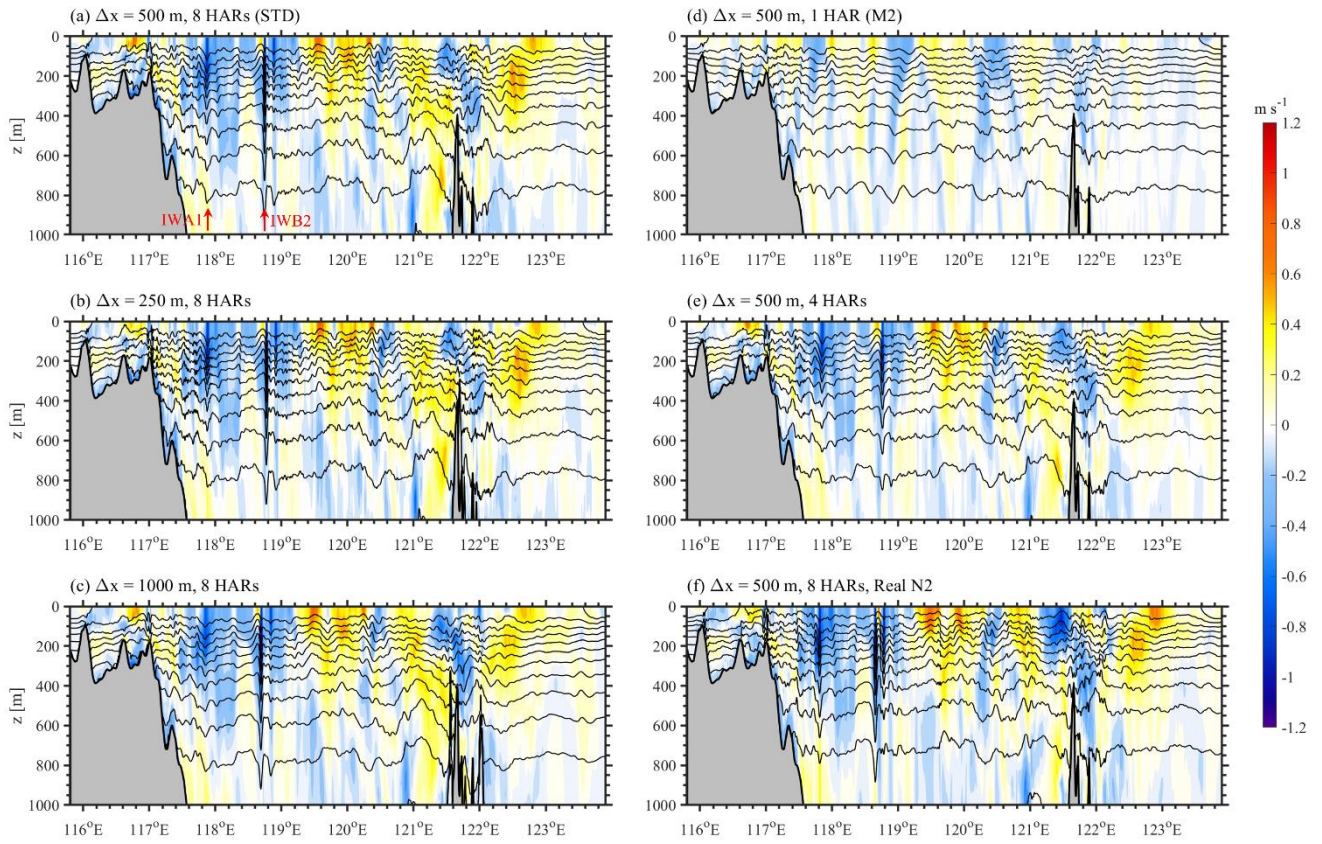
Figure 7. Temperature isotherms (contours) and baroclinic velocities (shades) along the transect (dashed line in Fig. 6a) at 12:00 UTC on 12 August 2014 in the model (a) ***500m_8HARs***, (b) ***250m_8HARs***, (c) ***1000m_8HARs***, (d) ***500m_1HAR***, (e) ***500m_4HARs***, and (f) ***500m_Real_N2***. Note that waves IWA1 and IWB2 are labelled in (a) with red arrows.
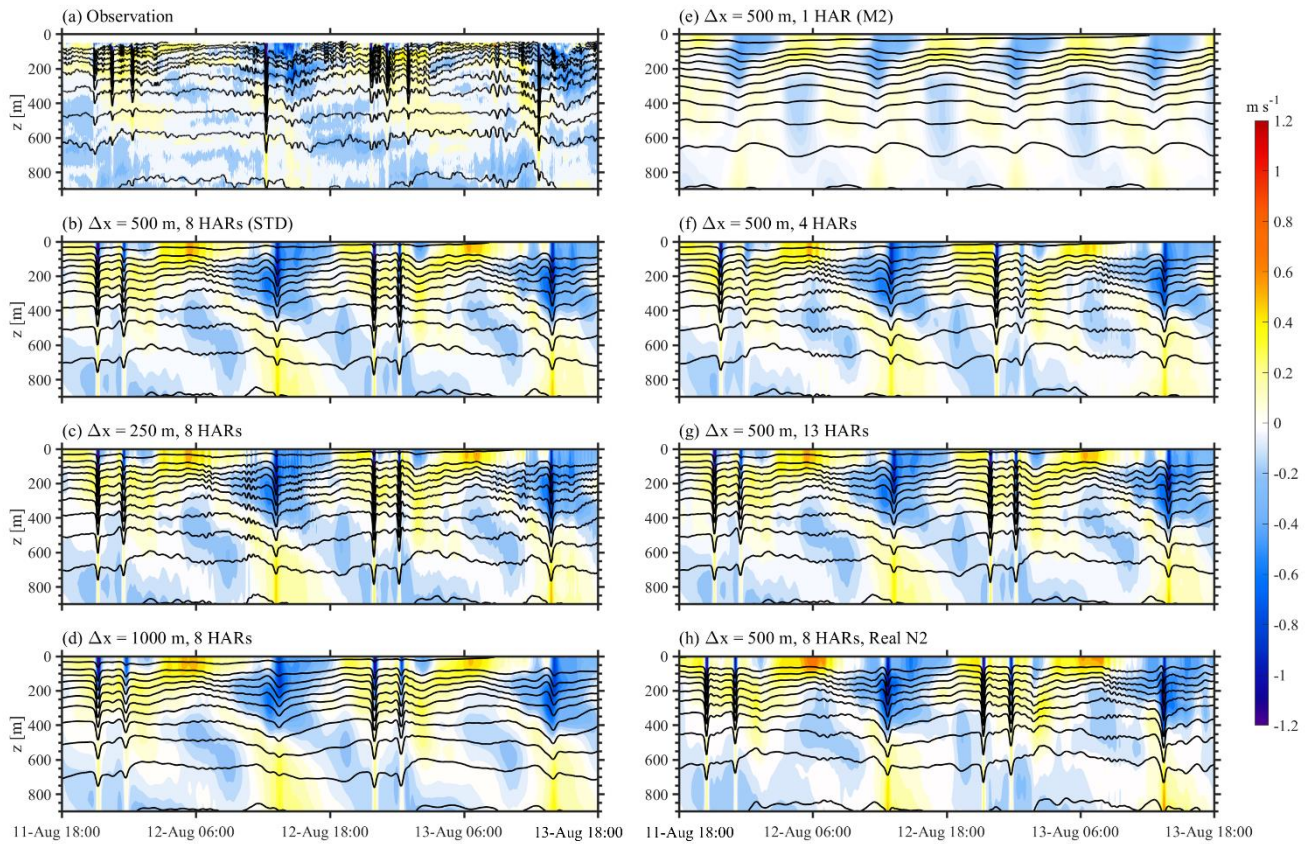
640

Figure 8. Time series of temperature isotherms (contours) and baroclinic velocities (shades) at station DS from 18:00 UTC on 11 August to 18:00 UTC on 13 August 2014 in the observation (a) and in the model (b) *500m_8HARs*, (c) *250m_8HARs*, (d) *1000m_8HARs*, (e) *500m_1HAR*, (f) *500m_4HARs*, (g) *500m_13HARs*, and (h) *500m_Real_N2*.
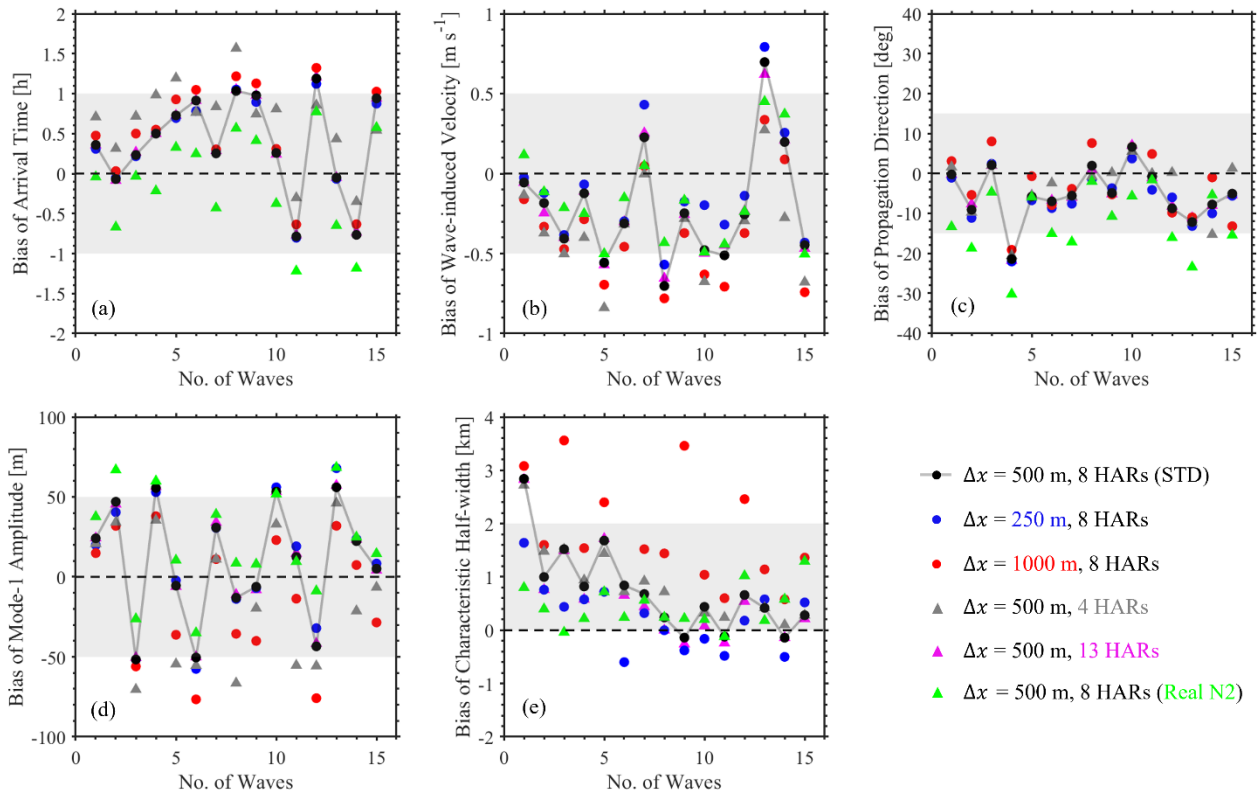
645 **Figure 9.** Bias of arrival time (a), maximum wave-induced velocities (b), propagation directions (c), maximum mode-1 wave amplitudes (d), and characteristic half-widths (e) for fifteen ISWs at station DS. Colours present different experiments.
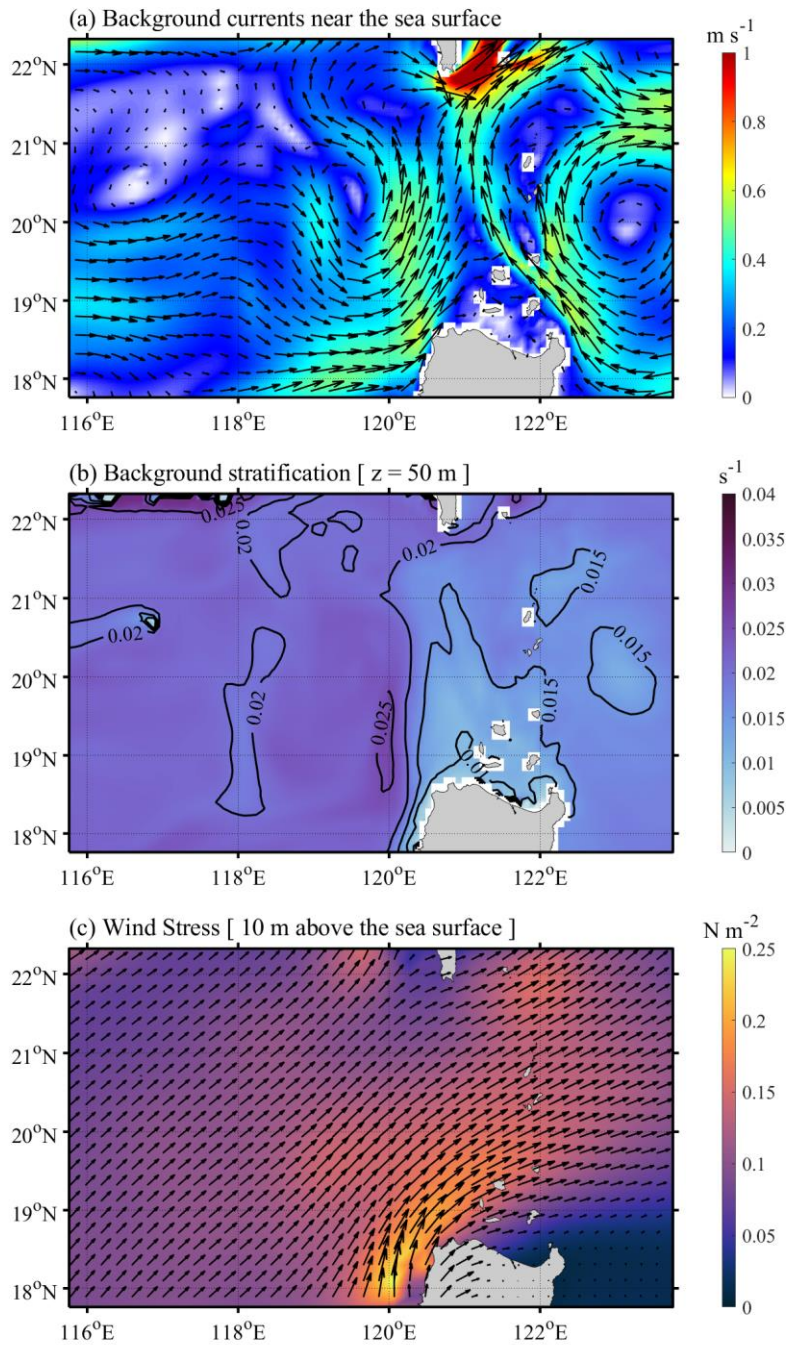
Figure 10. (a) Background currents near the sea surface (averaged from 05-AUG to 20-AUG 2014, derived from the global HYCOM dataset). (b) Background buoyancy frequency at a water depth of 50 m. (c) Time-averaged wind stress at 10 m above the sea surface, which is derived from NCEPv2 hourly dataset.

650
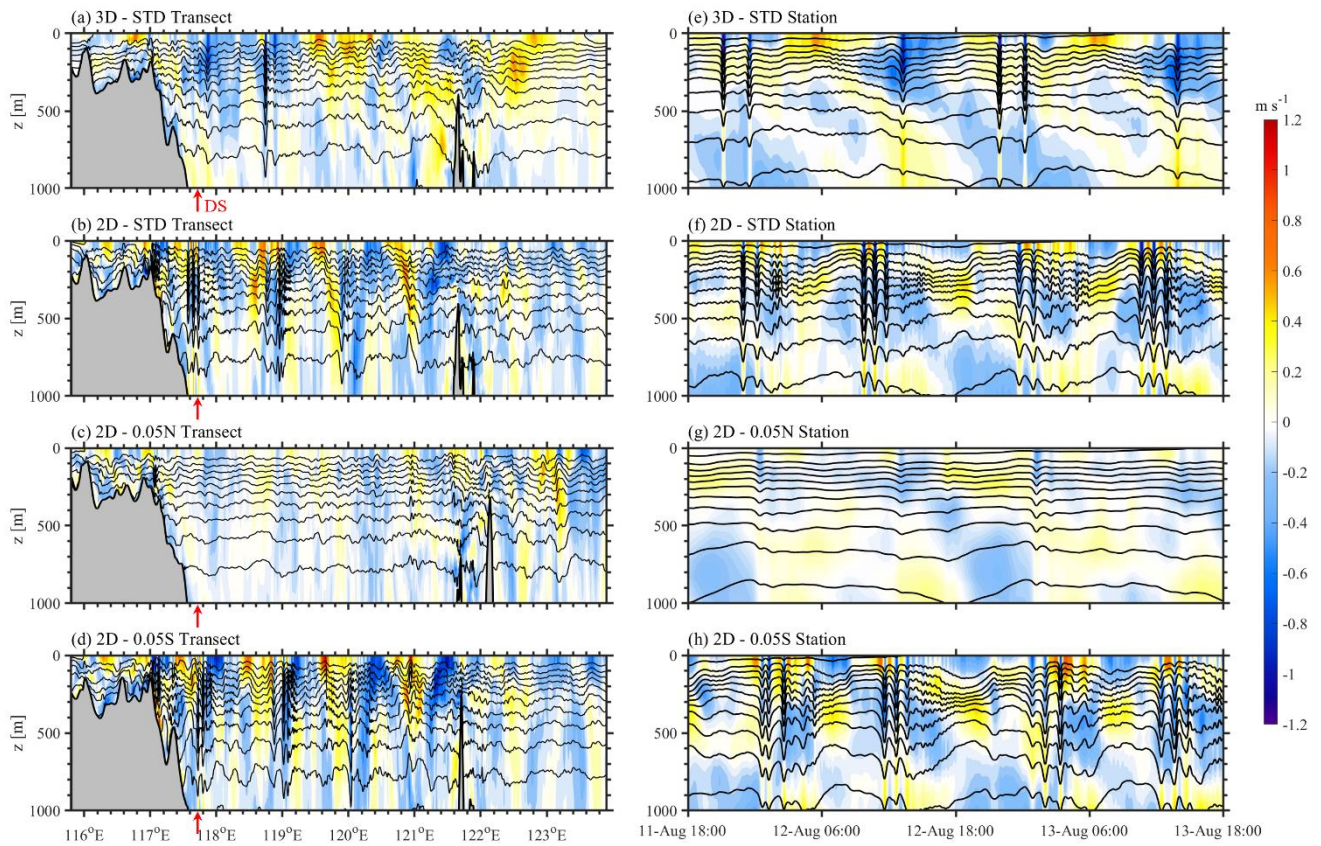
Figure A1. Temperature isotherms (contours) and baroclinic velocities (shades) along the transect at 12:00 UTC on 12 August 2014 in the 3D model (a) ***500m_8HARs***, in the 2D model (b) ***2D_500m_8HARs***, (c) ***2D_500m_8HARs_005N***, and (d) ***2D_500m_8HARs_005S***. (e – h) Corresponding time series at the stations, which are marked as red arrows in (a – d).
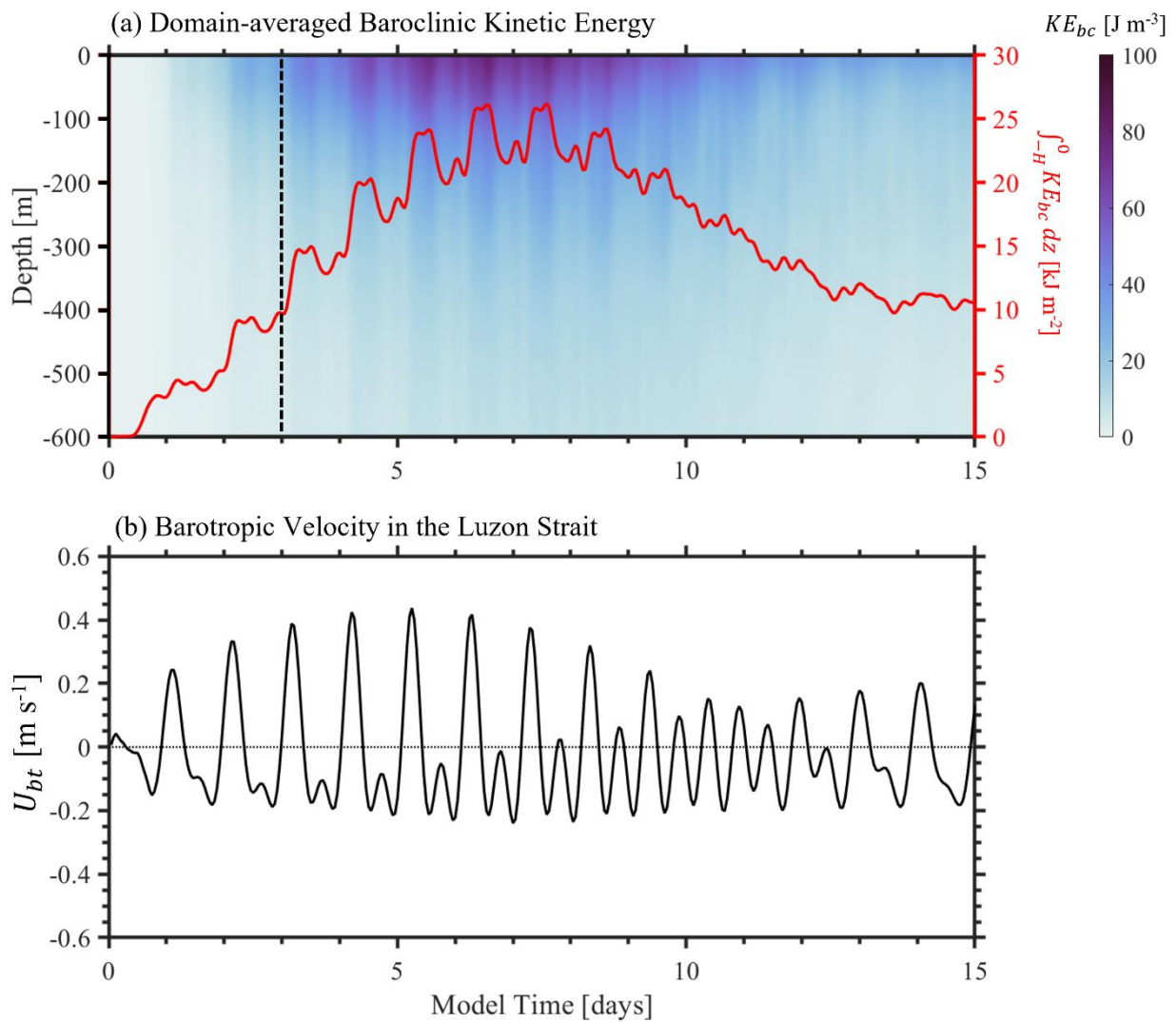
660 **Figure B1.** (a) Domain-averaged baroclinic kinetic energy (KE_{bc}, in the unit of J m^{-3}) in the inner model domain. Note that the red solid line is domain-averaged depth-integrated KE_{bc} ($\int_{-H}^{0} KE_{bc}\, dz$, in the unit of kJ m^{-2}). (b) Time series of barotropic velocity in the Luzon Strait.
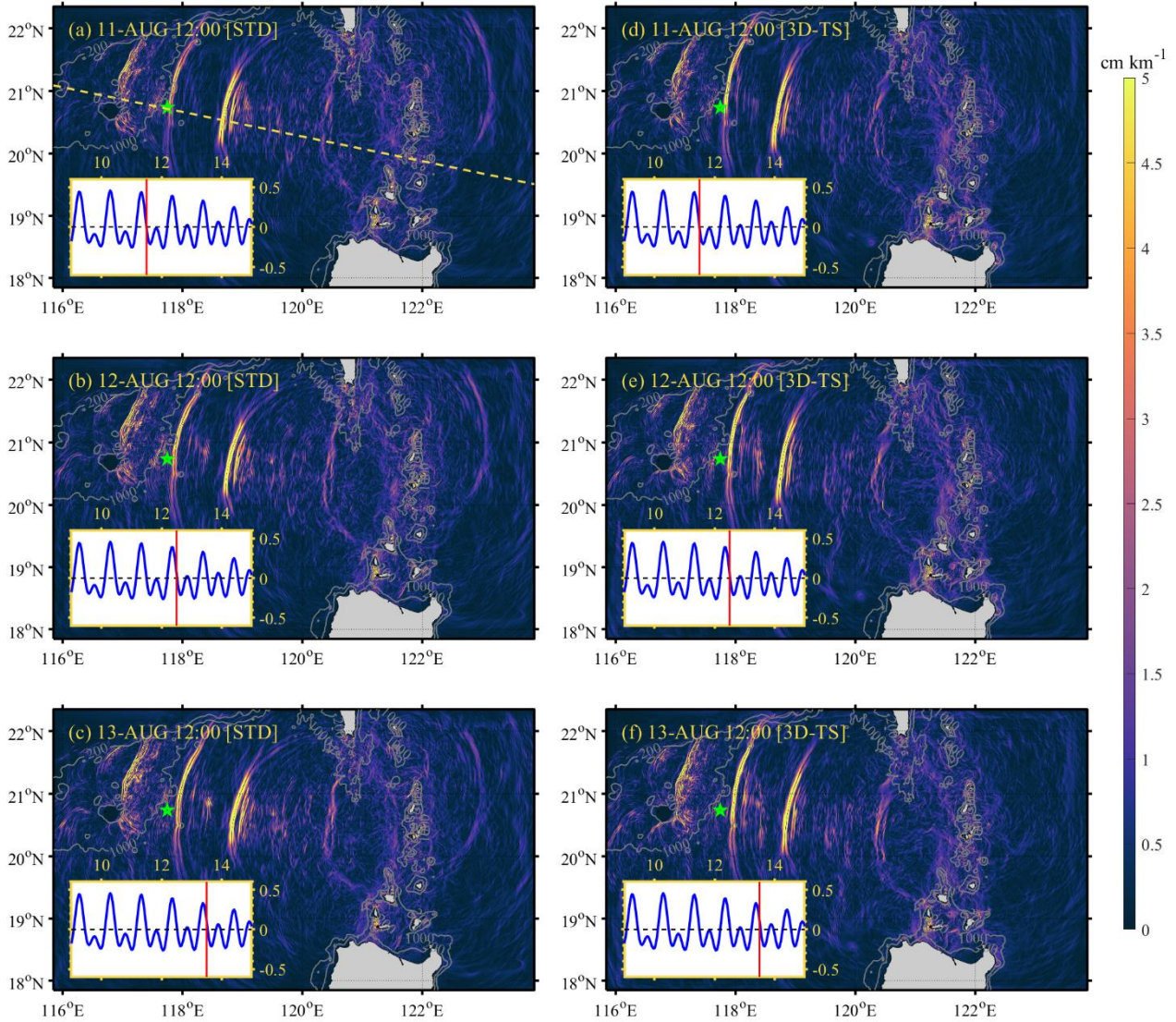
Figure C1. (a-c) Snapshots of sea surface gradients ($|\nabla\eta|$) at 12:00 UTC on 11, 12 and 13 August in the standard experiment
(EXP. *500m_8HARs*), respectively. (d-f) Same as (a-c) but in the sensitivity experiment with horizontally inhomogeneous
temperature and salinity (EXP. *3D-TS*).
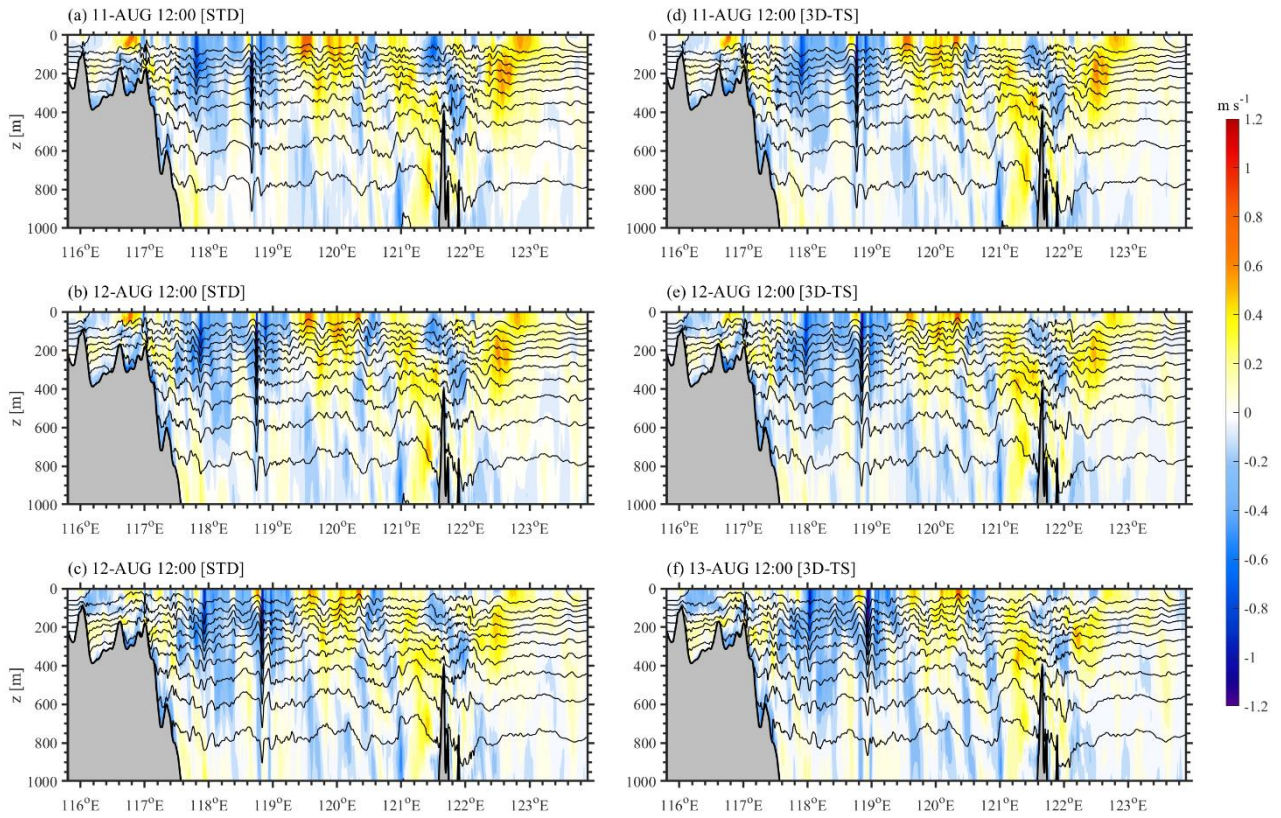
Figure C2. (a-c) Temperature isotherms (contours) and baroclinic velocities (shades) along the transect (dashed line in Figure R1a) at 12:00 UTC on 11, 12 and 13 August in the standard experiment (EXP. *500m_8HARs*), respectively. (d-f) Same as (a-c) but in the sensitivity experiment with horizontally inhomogeneous temperature and salinity (EXP. *3D-TS*).

Table 1. Summary of previous 3D non-hydrostatic models for internal solitary waves in the northern South China Sea, which are discussed in the text. Further details can be found in the references.

References	Model	Resolution	Tidal constituents	Model domain
Vlasenko et al. (2010) Guo et al. (2011)	MITgcm	$\Delta x = 250$ m, $\Delta y = 1000$ m	8 HARs	$118.0^{\circ} - 122.5^{\circ}$E $20.0^{\circ} - 21.0^{\circ}$N
Zhang et al. (2011)	SUNTANS	~1358 m (75 – 4740 m)	8 HARs	$115.0^{\circ} - 124.0^{\circ}$E $18.0^{\circ} - 23.0^{\circ}$N
Alford et al. (2015)	MITgcm	250 m	8 HARs	$119.6^{\circ} - 122.3^{\circ}$E $18.8^{\circ} - 21.8^{\circ}$N
Lai et al. (2019)	FVCOM	~200 – 500 m (near the shoreline) ~3 km (shelf-slope region)	8 HARs	$105.0^{\circ} - 130.0^{\circ}$E $12.0^{\circ} - 30.0^{\circ}$N
Zeng et al. (2019)	MITgcm	$\Delta x = 150$ m, $\Delta y = 300$ m	8 HARs	$115.5^{\circ} - 124.5^{\circ}$E $17.5^{\circ} - 22.5^{\circ}$N

Table 2. Summary of all experimental configurations.

No.	Experiment name	Grid spacing	Tidal forcing	Stratification
1	*500m_8HARs*	500 m	8 HARs (M2, S2, N2, K2, K1, O1, P1, Q1)	WOA18
2	*500m_8HARs_BT*	500 m	8 HARs	-
3	*250m_8HARs*	250 m	8 HARs	WOA18
4	*1000m_8HARs*	1000 m	8 HARs	WOA18
5	*500m_1HAR*	500 m	1 HAR (M2)	WOA18
6	*500m_4HARs*	500 m	4 HARs (M2, S2, K1, O1)	WOA18
7	*500m_13HARs*	500 m	13 HARs (M2, S2, N2, K2, K1, O1, P1, Q1, M4, MS4, MN4, MM, MF)	WOA18
8	*500m_Real_N2*	500 m	8 HARs	DS Station

675

Table 3. Root mean square deviation (RMSD) of wave properties between field observation and 3D sensitivity simulations at the mooring station in the vicinity of the Dongsha Atoll.

No.	Experiment name	RMSD of arrival time [h]	RMSD of wave-induced velocity [m s⁻¹]	RMSD of propagation direction [º]	RMSD of mode-1 wave Amplitude [m]	RMSD of characteristic half-width [km]
1	*500m_8HARs*	0.71	0.41	8.35	37.27	1.07
2	*500m_8HARs_BT*	-	-	-	-	-
3	*250m_8HARs*	0.67	0.38	8.89	38.12	0.64
4	*1000m_8HARs*	0.79	0.49	8.54	40.28	2.41
5	*500m_1HAR*	-	-	-	-	-
6	*500m_4HARs*	0.81	0.58	8.22	43.69	1.10
7	*500m_13HARs*	0.71	0.40	8.23	37.36	1.01
8	*500m_Real_N2*	0.62	0.34	14.74	37.88	0.58